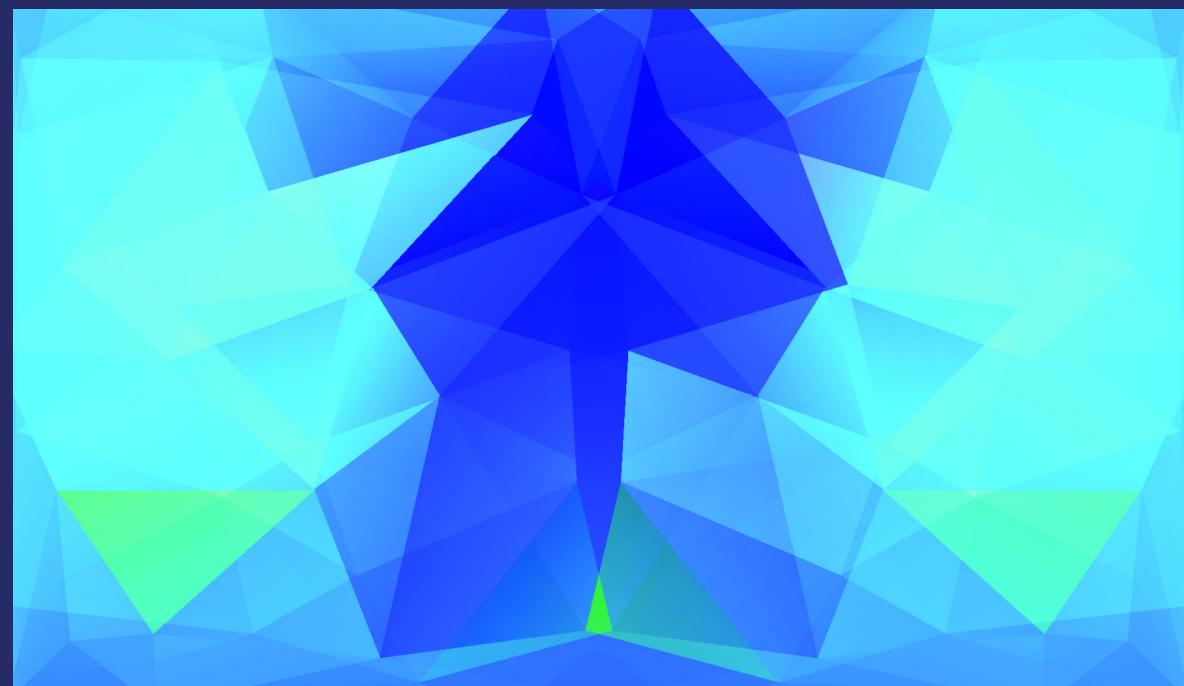


Photodynamic therapy (PDT) is a method of the treatment of localized cancers, based on a photochemical reaction between a light-activated molecule or photosensitizer (PS), light, and molecular oxygen. Correct choice of PS is of fundamental importance for PDT efficacy. Despite numerous studies in this field, most known PS have some drawbacks, e.g. lack of specificity and aggregation in aqueous media. Consequently, the search for an ideal PS is essential for further development of PDT. Here we review classification and analyze main features of different generations of PS and describe the mechanisms of their action. Various methods of targeted delivery of PS to tumor cells are discussed. The advantages of PS nanoparticles with the effect of aggregation-induced emission (AIE) over the classic photosensitizers are presented. A possibility of practical application of such light-emitting structures in cancer phototherapy is shown.



Irina Korotkova
Tamara Sakhno



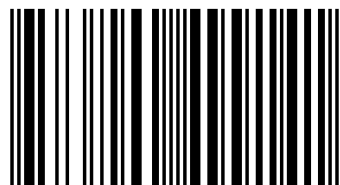
Irina Korotkova - Ph.D. in Physical Chemistry (June, 1998), Institute of Physical Chemistry NASU, Professor of the Department of Biotechnology and Chemistry, Poltava State Agrarian Academy, Ukraine.



Tamara Sakhno - Doctor of Chemistry, Professor of the Department of Biotechnology and Chemistry, Poltava State Agrarian Academy, Ukraine.

NANOPARTICLES WITH THE AGGREGATION-INDUCED EMISSION EFFECT: PROPERTIES AND APPLICATIONS

Photosensitizers for Photodynamic Therapy



978-620-0-49914-1

 **LAP**
LAMBERT
Academic Publishing

Irina Korotkova
Tamara Sakhno

**NANOPARTICLES WITH THE AGGREGATION-INDUCED EMISSION
EFFECT: PROPERTIES AND APPLICATIONS**

FOR AUTHOR USE ONLY

FOR AUTHOR USE ONLY

**Irina Korotkova
Tamara Sakhno**

**NANOPARTICLES WITH THE
AGGREGATION-INDUCED EMISSION
EFFECT: PROPERTIES AND
APPLICATIONS**

Photosensitizers for Photodynamic Therapy

FOR AUTHOR USE ONLY

LAP LAMBERT Academic Publishing

Imprint

Any brand names and product names mentioned in this book are subject to trademark, brand or patent protection and are trademarks or registered trademarks of their respective holders. The use of brand names, product names, common names, trade names, product descriptions etc. even without a particular marking in this work is in no way to be construed to mean that such names may be regarded as unrestricted in respect of trademark and brand protection legislation and could thus be used by anyone.

Cover image: www.ingimage.com

Publisher:

LAP LAMBERT Academic Publishing

is a trademark of

International Book Market Service Ltd., member of OmniScriptum Publishing Group

17 Meldrum Street, Beau Bassin 71504, Mauritius

Printed at: see last page

ISBN: 978-620-0-49914-1

Copyright © Irina Korotkova, Tamara Sakhno

Copyright © 2019 International Book Market Service Ltd., member of
OmniScriptum Publishing Group

FOR AUTHOR USE ONLY

NANOPARTICLES WITH THE AGGREGATION-INDUCED EMISSION EFFECT: PROPERTIES AND APPLICATIONS

Irina Korotkova, Tamara Sakhno

*Poltava State Agrarian Academy, 1/3, Skovorody Str., 36003, Poltava, Ukraine
Corresponding author: 2irinakorotkova10@gmail.com*

CONTENT:

	Abbreviations	2
1.	NANOPARTICLES CREATION, SPECTRAL-LUMINESCENCE PROPERTIES	3
2.	PHENOMENON OF THE AGGREGATION-INDUCED EMISSION, MECHANISMS	10
2.1.	Restriction of Intramolecular Rotation	12
2.2.	Restriction of Intramolecular Vibrations	26
2.3.	Restriction of Intramolecular Motion	28
3.	Fluorescent Properties of Aggregates of J-Type Molecules	29
4.	Luminescence of Pairs of Organic Ions and Transition Metal Complexes	34
5.	APPLICATIONS OF AGGREGATION-INDUCED EMISSION	37
5.1.	Luminescent Solar Concentrators	37
5.2.	Optoelectronic Applications.	38
5.3.	Environmental Monitoring	39
5.4.	Biological and Biomedical Applications	41
6.	PHOTODYNAMIC THERAPY	41
6.1.	Mechanism of Photodynamic Therapy	42
6.2.	Photosensitizers for Photodynamic Therapy	45
6.3.	Nanoparticles of Photosensitizers creation for Photodynamic Therapy	47
6.4.	Nanoparticles based on inorganic materials and organic materials	48
6.5.	Nanoparticles of photosensitizers with an aggregation-induced emission effect	50
	Conclusions	62
	References	63

Abbreviations

AEMA	2-aminoethyl methacrylate
ALA	5-aminolevulinic acid
AlPc	aluminum-phthalocyanine chloride
AlPcS4	aluminium phthalocyanine tetrasulphonated (Photosens)
AlS2Pc	disulfonated phthalocyanine
BDP	boron dipyrromethene
BHQ3	black hole quencher3
BSA	bovine serum albumin
c(RGDfc)	Arg-Gly-Asp-d-Phe-Cys cyclic peptide
cRGD	cyclic arginine-glycine-aspartic acid
DCF-DA	dichlorofluorescein diacetate
DMSO	Dimethyl sulfoxide
DPBA-TPE	(3,3'-(2,5-dimethoxy-1,4-phenylene)bis(2-(4-bromophenyl)acrylonitrile)-tetraphenylethene
DSPE-PEG-Mal	1,2-distearoyl-sn-glycero3-phosphoethanolamine-N-[maleimide(polyethylene glycol)]
DTPEBBTD	Donor- tetraphenylethene- benzo[1,2-c:4,5-c']bis([1,2,5]thiadiazole)
DMF	dimethylformamide
GFLG	Gly-Phe-Leu-Gly-peptide
HPMA	<i>N</i> -(2-hydroxypropyl)methacrylamide
m-THPP	meta-tetra(hydroxyphenyl)porphyrin (Foscan)
PEG	polyethylene glycol
PLGA	poly(lactic-co-glycolic acid)
PLGVR	Pro-Leu-Gly-Val-Arg-peptide
PpIX	protoporphyrin IX
PMMA	polymethyl methacrylate
PVM/MA	poly(methyl vinyl ether-co-maleic anhydride)
ROS	reactive oxygen species

TICT	Twisted Intramolecular Charge Transfer state
TPA FN	2,3-bis[4-(diphenylamino)phenyl]fumaronitrile
TPE-red	2-((4-(2,2-bis(4-methoxyphenyl)-1-phenylvinyl)phenyl)(phenyl)methylene)malononitrile
TPE-TPA-DCM	2-(2,6-bis((<i>E</i>)-4-(phenyl(4'-(1,2,2-triphenylvinyl)-[1,1'-biphenyl]-4-yl)amino)styryl)-4 <i>H</i> -pyran-4-ylidene)malononitrile
TPETPA FN	2,3-bis(4-(phenyl(4-(1,2,2-triphenylvinyl)phenyl)amino)phenyl)fumaronitrile
TPPS4	5,10,15,20-tetrakis(4-sulfanatophenyl)-21H,23H-porphyrin
TPEPy-TEG	(<i>E</i>)-4-(4-(2,2-bis(4-(2-(2-(2-hydroxyethoxy)ethoxy)ethoxy)phenyl)-1-phenylvinyl)styryl)-1-methylpyridin-1-ium
TTD	(2-(2,6-bis((<i>E</i>)-4-(phenyl(4'-(1,2,2-triphenylvinyl)-[1,1'-biphenyl]-4-yl)amino)styryl)-4 <i>H</i> -pyran-4-ylidene)malononitrile
UCNPs	upconversion nanoparticles

1. NANOPARTICLES CREATION, SPECTRAL-LUMINESCENCE PROPERTIES

Intensively fluorescent nanoparticles of inorganic and organic materials have attracted great interest of researchers in the last two decades due to their unique properties, caused, in particular, by quantum-dimensional effects [1, 2]. Such nano-objects have found wide application, including as fluorescent biological labels, active elements of light-emitting devices, etc. [3-5].

Nanoparticles of organic molecules, in comparison with their inorganic analogues, suggest greater variability in structure and physical properties. Their chemical and photochemical stability is higher than for isolated molecules and they demonstrate unique optical and optoelectronic properties and are of considerable interest for various potential applications in the creation of new biological sensors (probes, tags) [6], organic light-emitting devices [7,8] and many others. But, only some of these objects emit strong fluorescence. Most organic luminophores with strong fluorescence in solution at low concentrations have much lower emission efficiency in the solid state. The formation of excimers, generation of excitons, and

the migration of excitation energy to impurity sites or surface defects in solid structures sharply decrease the emission efficiency.

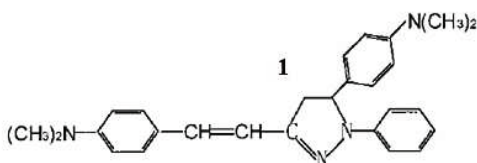
However, in recent years, there are a number of compounds have been established for which enhanced fluorescence due to aggregation of luminophore molecules in solutions or in an adsorbed state is observed. Such effects were observed in a study of organosilicon compounds: penta- and tetraphenylsilols, 1-methyl-1,2,3,4,5-pentaphenylsilol [9, 10], silol-containing polyacetylenes [11], as well as other derivatives of arylolethynyl [12], poly(phenyleneethynylene) [13], poly(phenylenevinylene) [14], 1,4-*bis*(phenylethynyl)benzene [15], pyrazoline [16], 1-cyano-trans-1,2-*bis*(4'-methylphenyl)ethylene [17], 2,2'-dihydroxyazine, and barbituric acid [18-20]. Covalently-bound dimers, namely, biscyanine dyes with conjugated chromophores, showed a previously unknown effect, namely, an enhanced fluorescence yield along with enhanced intersystem crossing (ISC) [21]. Such a paradox can be attributed to a greater probability for radiative transition in comparison with nonradiative transition with increasing angle between the chromophores. The increase in the probability of triplet states population upon the interaction of the chromophores in biscyanines has been used to obtain intense fluorescence in the near-IR spectral region due to thermoactivation of slow luminescence [22].

The effect of enhanced fluorescence due to aggregation of luminophore molecules leads to a significant change in their fluorescence properties [23, 24], including an increase in the fluorescence quantum yield [25].

When creating nanoparticles based on organic materials, it should be note that their fluorescence properties depend on the nanoparticles size. This dependence was first described for nanoparticles of perylene and phthalocyanine by Kasai et al. [26-29]. Thus, three types of bands [26, 28] identified as monomer luminescence ($\lambda_{fl} = 440$ nm), F-exciton emission ($\lambda_{fl} = 480$ nm), and S-exciton emission ($\lambda_{fl} = 560$ nm) (where F is a free exciton and S is a self-trapped exciton) are observed in the emission of perylene crystals varying in diameter from 93 to 211 nm. For crystals with diameter 50 nm, the F-exciton emission band maximum is found about 470 nm,

while for particles with diameter 200 nm, the maximum is at 482 nm [27]. Furthermore, decreasing crystal size leads to an increase in the intensity of F-exciton emission relative to the intensity of S-exciton emission.

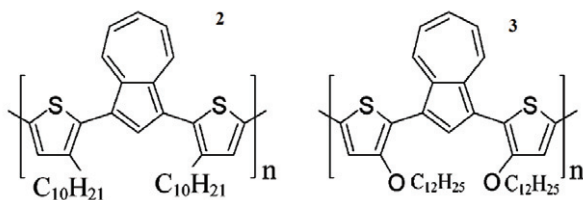
The spectral-luminescent properties of 1-phenyl-3-(dimethylamino)styryl)-5-((dimethylamino)phenyl)-2-pyrazoline (**1**) also depend on the nanoparticles size.



Thus, increasing the diameter from 20 to 310 nm leads to the appearance of a charge transfer (CT) band in the absorption spectrum, which bathochromic shifts from 438 to 455

nm [17]. A band with maximum at 450 nm is observed in solution of **1** in ethanol. An emission bands with maximum at $\lambda_{fl} = 500, 535,$ and 463 nm arise in the presence of nanoparticles of **1**, the intensity of bands gradually decreases with increasing nanoparticle size. The redistribution of the emission intensity from the S_1 state to the state with CT with increasing nanoparticle size indicates that these states compete with each other [30-36].

Strong dependence of the absorption intensity and significant enhancement of the emission with increasing particle size were observed for monodisperse conjugated polymer nanoparticles of poly{1,3-bis[2-(3-*n*-decylthienyl)]azulene} (**2**) (Fig. 1) and poly{1,3-bis[2-(3-*n*-dodecoxythienyl)]azulene} (**3**) [37].



As follows from the presented dependences an increase in the nanoparticles size occurs during the aging which is accompanied by a change in emission properties of **2**.

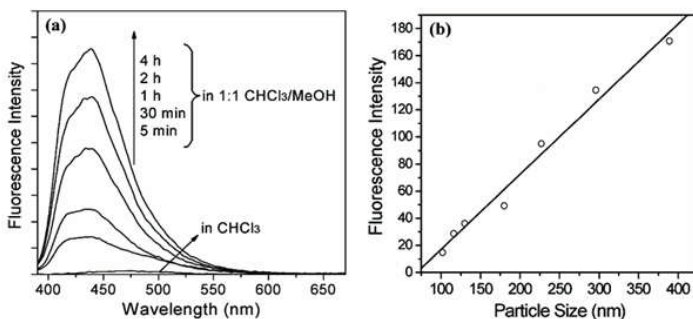
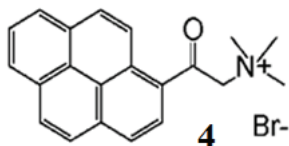


Fig. 1. a) Fluorescence spectra of nanoparticles of **2** in CHCl_3 and in $\text{CHCl}_3/\text{CH}_3\text{OH}$ mixture (1:1) at variable time intervals, b) size dependence of the fluorescence intensity of nanoparticles of **2**. Reprinted with permission [37]. Copyright © 2005, American Chemical Society.

A study of nanoaggregates of trimethyl(2-oxo-2-pyren-1-ylethyl)ammonium bromide (**4**) in tetrahydrofuran (THF) in the presence of added water showed that their fluorescent properties depend not only on the dye concentration but also on the size of its nanoparticles.

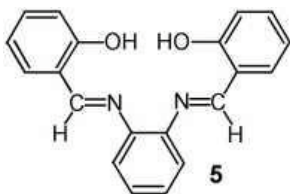


The spectra of dilute solutions of **4** have fluorescence bands with maxima at $\lambda_{fl} = 309, 412, \text{ and } 433 \text{ nm}$, which shift with increasing dye concentration toward longer wavelengths and coalesce into a single broad band with $\lambda_{fl} = 469 \text{ nm}$. The observed spectral changes are related to the formation of nanoparticles of **4** and change in their size upon increasing the dye concentration. Furthermore, the position of the fluorescence bands and size of the nanoparticles of **4** formed depend also on the $\text{H}_2\text{O}/\text{THF}$ ratio in the mixture. Thus, an increase in the water content leads to a shift in the fluorescence maximum from $\lambda_{fl} = 433$ to 448 nm obtained by the addition of 0.5 mL aqueous solution of **4** to 0.5 mL THF and the appearance of a ball-shaped aggregate with diameter 450 nm [38].

A similar dependence of the fluorescent properties of **4** on its content was also observed in polyvinyl alcohol films. At low dye content ($0.01 \text{ mole } \%$), only emission of the monomer form at 450 nm is observed, but the fluorescence maximum

is shifted with increasing concentration to 2.0 mole % toward longer wavelengths ($\lambda_{fl} = 530$ nm), which is attributed to the emission of dimers or excimers of **4** [39-41].

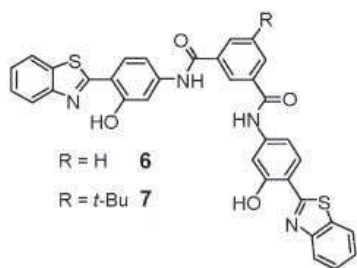
The particles aging leads to an increase in their size and greater ordering of crystal structure, which is accompanied by change in the emission properties. Thus, an increase in the fluorescence of *bis*(salicylaldehyde)-*o*-phenylenediimine



(salophen) (**5**) is found upon the addition of dioxane solution to water [36]. This behavior is related to the formation of microtubes of salophen. In the initial step, these structures are formed with the participation of primary disordered rod-like nanoparticles with diameter

80-120 nm and length 400-600 nm, which convert over 1 h into semi-tubular structures. The formation of the microtubes is accompanied by a sharp change in the fluorescence intensity. The emission spectra of the solution of **5** in dioxane and the initial suspension of nanoparticles have two weak bands with maxima at 545 and 435 nm. Upon aging, the intensity of the emission at 545 nm decreases and the shorter-wavelength band undergoes a bathochromic shift to 451 nm and its intensity gradually undergoes a more than 100-fold increase. The driving forces for the self-organization of these parties and their combination with microtubes formation may be multiple intermolecular C-H $\cdots\pi$ interactions, which provide rigidity to the molecular structure such that “tubular” salophen becomes a stronger emitter. The mechanism of this process is similar to the similar mechanism of “oriented binding” in the formation of nanorods of anatase (TiO₂) [42].

The differences in the emission of N,N'-di[3-hydroxy-4-(2'-benzothiazole)phenyl]isophthalic amide (**6**) and N,N'-di[3-hydroxy-4-(2'-benzothiazole)phenyl]5-ferEbutyl-isophthalic amide (**7**) solutions are explained by different models of molecular stacking and the shape of the resultant aggregates, which confirmed by the time-dependent recording of the fluorescence spectra of the nanoparticles/aggregates (Fig. 2) and molecular modeling [43].



Two bands of unequal intensity are also observed in the emission spectra of **6** and **7** in THF. Weak band at 393 nm is attributed to emission of the enol, and the band at 509 nm is related to the keto-tautomer formed as a result of excited-state intramolecular proton transfer (ESIPT), which

takes place with quantum yield 0.0021 for **6** and 0.0017 for **7** at room temperature.

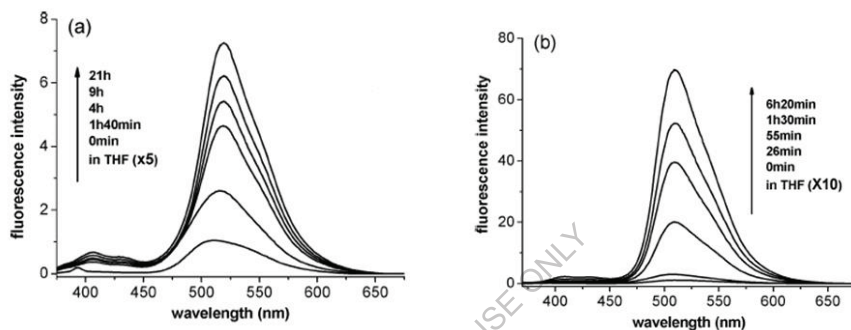


Fig. 2. Time-dependent evolution of the fluorescence spectra of **6** (a) and **7** (b) in THF and in THF/H₂O mixture (38:62 vol.) at variable time intervals. Reprinted with permission [43]. Copyright © 2007, American Chemical Society

The addition of water to THF with the same dye concentration leads to increased emission of both compounds due to changes in the shape and size of the nanoparticles. Thus, the particle diameter of **6** is about 100 nm after 2 h and 150-250 nm after 4 h, while cubic particles with spherically-ordered arrangement of molecules of **6** form after 21 h. The growth of aggregates of **7** is much more rapid: particle diameter is 20-150 nm after 15 min and 100-400 nm after 30 min, while large rectangular rods with length 280-580 nm and width ~ 80 nm are formed after 1 h.

The changes in shape and size of the nanoparticles also affect their spectral characteristics. Thus, the luminescence intensity of **7** upon its solution aging in THF/H₂O gradually increases with invariant position of the fluorescence maxima attributed to the keto-form. After solution aging for 6 h, the emission quantum yield increased to 0.19, i.e., by a factor of about 112 to the fluorescence in pure THF ($\phi \approx$

0.0017) and by a factor of 21 to the emission intensity of **7** in THF/H₂O mixture ($\phi \approx 0.009$). The band intensity at 393 nm attributed to the fluorescence of the enol also increased 9-fold relative to the initial sample. The solution aging of **6** in THF/H₂O mixture (38:62 vol.) was accompanied by an increase in emission quantum yield from $\phi \approx 0.012$ ($\lambda_{fl} = 516$ nm) to $\phi \approx 0.029$ ($\lambda_{fl} = 519$ nm) at ripening times of 21 h [43].

Compound **8** is a prominent representative of coumarin derivatives. Coumarin derivatives are most attractive chromophores for their excellent properties, such as high fluorescence quantum yield, large Stokes shift, less toxicity, ease of modification and visible wavelength emission. The spectral-luminescence properties of coumarine derivatives are presented in studies [44-46].

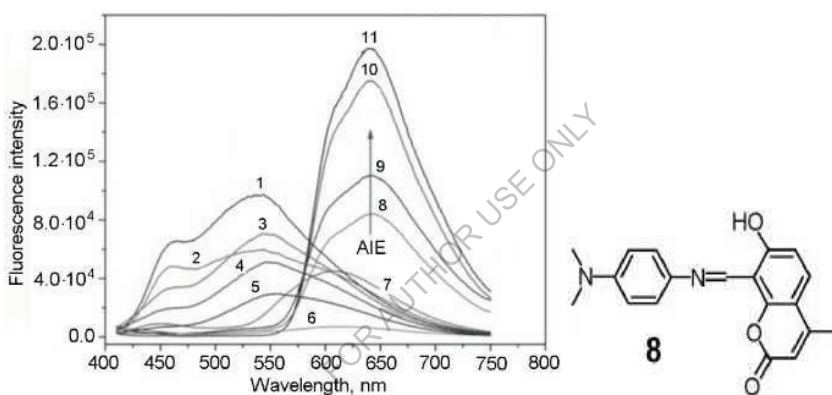
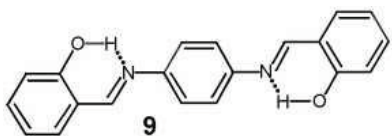


Fig. 3. Fluorescence spectra of **8** in H₂O/DMF mixtures with water content: 0 (1), 10 (2), 30 (3), 40 (4), 20 (5), 50 (6), 60 (7), 70 (8), 80 (9), 90 (10), and 99 vol.% (11). Reprinted with permission [47]. Copyright © 2016, The Royal Society of Chemistry.

As a result of the ESIPT process, highly luminescent aggregates of different size are formed for 8-((4'-dimethylamino-2'-ylimino)-methyl)-7-hydroxy-4-methyl-2H-chromen-2-one (**8**), in which the proton donor (-OH) and proton acceptor groups (-C=N-) are rather close to each other. The observed red shift of the fluorescence band ($\lambda_{fl} = 604$ nm in ethanol to $\lambda_{fl} = 650$ nm in the film) is attributed to the aggregates formation of **8**, in which rotation of the phenyl group is hindered. The aggregates formation of **8** was observed in H₂O/DMF mixture with various water fractions. Figure 3 shows that increasing the water content to 50% leads to a decrease

in the fluorescence intensity, which is related to intramolecular charge transfer in the folded conformation of the compound arising in the excited state. Enhanced emission is observed at the water content in the mixture exceeds 60% along with a shift in the emission maximum from 540 to 640 nm. The red shift and enhanced emission are attributed to aggregates formation of **8** due to hindrance of C=N isomerization and rotation of the phenyl group, which favor the ESIPT process [47].

The conversion of particles of N,N'-bis(salicylidene)-*p*-phenylenediamine (**9**) from nanospheres with diameter 10 nm into rod-like structures with length about 2000 nm and width 100 nm is accompanied by a more than 60-fold enhancement of fluorescence intensity in comparison with the intensity of this compound in methanol solution [48].



We should note that the fluorescence band of **9** in CH₃OH has maximum at $\lambda_{fl} = 535$ nm, while this band appears in water at $\lambda_{fl} = 546$ nm. The band intensity depends on the aging time: the quantum yield drops from $\phi \approx 0.06$ to $\phi \approx 0.025$. The reason for this change in emission during aging of the sample is not completely clear but may be related to an interaction involving the azomethine group of one molecule with the benzene ring of another in the nanoparticle [48].

Next we will consider the spectral-luminescent properties of aggregates and nanoparticles of organic compounds named AIE luminogens and the possibility of using the aggregation-induced emission (AIE) effect in light emitting structures.

2. PHENOMENON OF THE AGGREGATION-INDUCED EMISSION, MECHANISMS

The luminogens (called AIEgens) are non-emissive as molecules, but when aggregates are formed, they become emissive [49]. This phenomenon was first reported in 2001 by Tang et al. in the study [9]. In 2002 Park et al. reported aggregation-induced enhanced emission (AIEE) in similar materials [17].

Several mechanisms have been hypothesized to explain aggregation-induced emission (AIE). In early reports, the mechanism of the Restriction of Intramolecular Rotations (RIR) first proposed by Chen et al. [10] was popular. Other mechanisms based on the Restriction of Intramolecular Vibrations (RIV) and Restriction of Intramolecular Motion (RIM) [49] also have been proposed. In recent decades, mechanisms involving photoinduced electron transfer, intermolecular charge transfer, fluorescent inductive resonance energy transfer, charge transfer from ligands to metal, formation of excimers and exciplexes, as well as the above mentioned ESIPT also have been proposed. Realization of all these mechanisms reduces predominantly to restriction to molecular motion such as rotation, vibration, and conformational change such that the nonradiative changes for the degradation of excitation energy is blocked and self-quenching is suppressed due to the effect of the medium (change in the solvent nature, viscosity, and temperature), which results in the formation of aggregates with bright emission.

A mechanistic picture for the AIE process can be represented as restriction of dynamic intramolecular motions, namely, low-frequency vibrational and rotation modes of energy reorganization involved in the nonradiative dissipation of the excited state energy of an AIE luminogen. The efficiency of radiative channels for the dissipation of electronic excitation energy and emission intensity is enhanced due to restriction of such motion. Whether a luminogen will possess an AIE effect depends largely on the conformational flexibility and amplitude of the motions of its molecules. The quenching of the emission of solutions is a key factor in the AIE of a structurally-flexible luminogen, which is the result of the consumption of energy required to perform intramolecular motions. AIE luminogens, as a rule, are nonplanar molecules not displaying luminescent properties as isolated molecules. Thus, it was considered until recently that a poor light emitter in the dissolved state cannot emit efficiently in the solid state. However, AIE shows that this concept is not always correct. A weak emitter in a dilute solution can be an efficient emitter in the solid state. This finding expands the scope of the search for efficient light-emitting solid materials, which may be employed in nanophotonic devices for various purposes.

2.1. Restriction of Intramolecular Rotation

The major structural feature of organic molecules, which demonstrate a unique improvement of emission in the solid state due to the restriction of intermolecular rotation, is the presence of fragments capable of rotation about C-C, C-N, or N-N single bonds. Nile red and carbocyanines are such molecules. Although only the contribution of intramolecular rotation is considered in explaining their optical properties, other types of motion such as vibrations including bending and twisting should also be taken into account since such motions use excited state energy [50].

Rotation around the C-C bond. The mechanism based on the restriction of intramolecular rotation was first proposed by Chen et al. [11] on the basis of the study results of a typical AIE fluorophore, 1,1,2,3,4,5-hexaphenylsilol (**21**). The silol ring in this molecule is bonded to six phenyl rings by single bonds, which imparts conformational rigidity, and this molecule may take a propeller-like conformation [51]. As a consequence of a strongly twisted conformation due to the steric repulsion of adjacent phenyl groups, dense head-to-tail packing of these molecules is impossible and there is no π - π stacking interaction in the solid state. However, C-H \cdots π interactions arise between molecules of **21** with short contacts (2.57-3.642 Å), which stabilize the crystal packing and restrict rotation of the phenyl groups [49].

Hexaphenylsilol **21** is highly soluble in organic solvents such as THF, chloroform, acetonitrile, and acetone, less soluble in methanol, and insoluble in water. Thus, water is used as a precipitating agent causing aggregation of molecules of **21** in solvents with added water such as in aqueous acetone. A dilute solution of **21** in acetone has a low fluorescence quantum yield ($\phi \approx 0.001$). The value of ϕ hardly changes as long as the water fraction in acetone/ water mixture does not exceed ~ 50 vol %, but then steadily rises with increasing water fraction. When the water content is ~ 90 vol %, the quantum yield rises to 0.22, which is ~ 220 fold higher than that of the pure acetone [11].

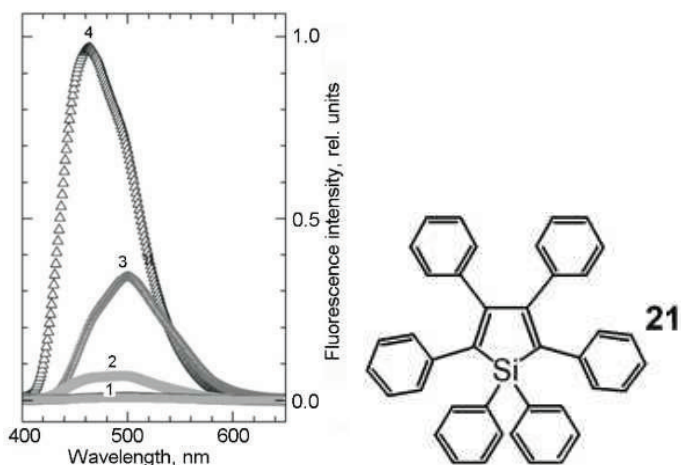


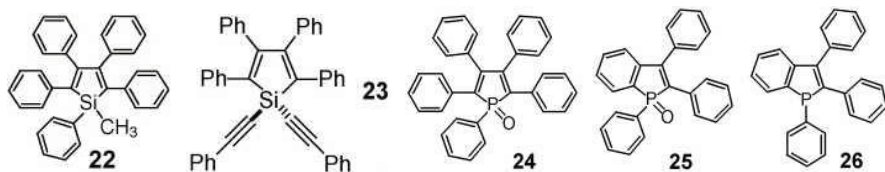
Fig. 4. Fluorescence spectra of **21** in THF/H₂O with water content 0-60 (1), 80 (2) ($\lambda_{fl} = 485$ nm), 90 (3) ($\lambda_{fl} = 500$ nm), and 70 vol.% (4) ($\lambda_{fl} = 462$ nm). Reprinted with permission [52]. Copyright © 2006, Elsevier

Similar trends in the change of luminescence properties were also found in solutions of **21** in THF/H₂O mixture (Fig. 4) with an increase in the emission quantum yield from 0.0015 in pure THF to 0.003, 0.35, and 0.13 in mixtures with 60%, 70%, and 90% water, respectively. Bhongale et al [52] have shown that the observed enhancement of fluorescence in solutions with increasing water content in THF/H₂O mixture is related not only to the AIE effect but also depends on the structure morphology (nanocrystals, nanoglobules, and microglobules), which may form in these systems.

A study of the fluorescence of **21** in glycerin/methanol mixtures [11] showed that the emission intensity of this compound also is enhanced in solutions with higher viscosity. Thus, the emission intensity of **21** in glycerin/methanol (50:50) is 5-fold higher than in pure methanol. The greater viscosity of the solution restricts intramolecular rotation similar to cooling, which hinders thermoactivated intramolecular rotation [12].

An increase in the luminescence intensity of **21** and 1-methyl-1,2,3,4,5-pentaphenylsilol (**22**) with increasing aggregation of these compounds was also observed in water/ethanol solutions [10, 52]. In particular, the fluorescence quantum

yield of **22** in water/ethanol (90:10) is 0.21, which is 333-fold higher than in pure ethanol ($\phi = 0.63 \cdot 10^{-3}$).



Enhanced fluorescence intensity in solution of 1,1-*bis*(phenylethynyl)-2,3,4,5-tetraphenylsilole (**23**) in dioxane was observed with decreasing temperature due to restriction of thermally activated intramolecular rotation (Fig. 5A)[11]. Cooling of silole solution in THF to $-196\text{ }^{\circ}\text{C}$ led to an increase in the fluorescence intensity of ~ 360 -fold in comparison with emission at room temperature (Fig. 5B). The effect of temperature on the fluorescence intensity of solutions of a series of other multiatomic heteroaromatic molecules was described in our previous studies [53-55].

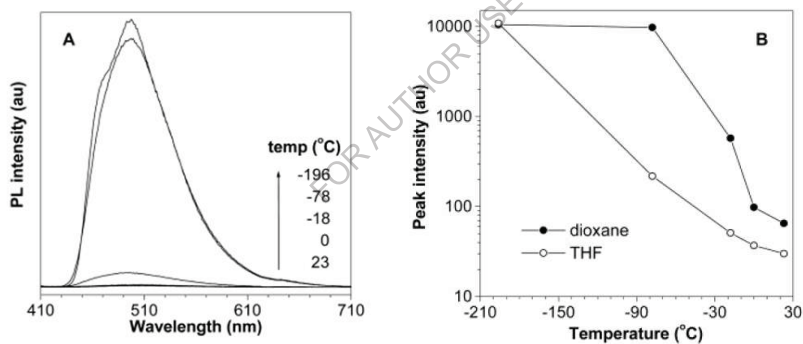


Fig. 5. Fluorescence spectra of **23** in 1,4-dioxane at different temperature (A); temperature dependence of the photoluminescence intensity of **23** in THF and in dioxane (B) ($C = 10\text{ }\mu\text{M}$, $\lambda_{\text{exc}} = 407\text{ nm}$). Reprinted with permission [11]. Copyright © 2003, American Chemical Society.

Similar to silole molecules, heterocyclopentadienyl derivatives such as 1,2,3,4,5-pentaphenylphosphole-1-oxide (**24**) [56], 1,2,3-triphenylphosphindole-1-oxide (**25**), 1,2,3-triphenylphosphindole (**26**) also display change in the spectral-luminescent properties upon variation of the components ratio in mixtures of organic solvents with water (Fig. 6).

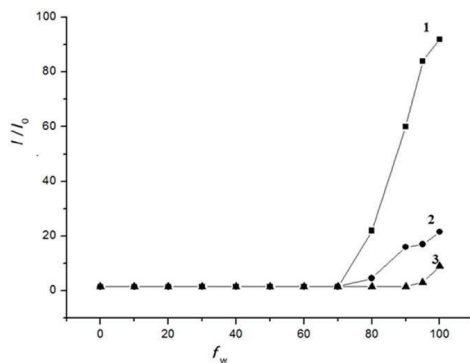
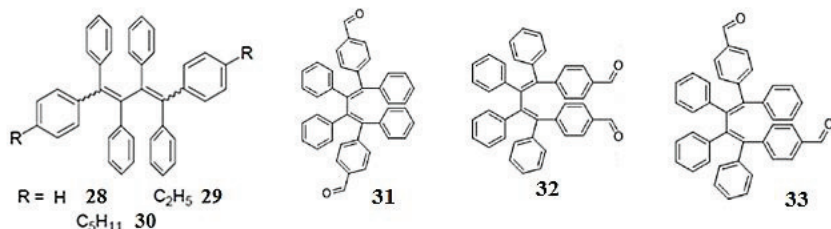


Fig. 6. The relative fluorescence intensity dependences of **24** (1), **26** (2), and **25** (3) on the water content (f_w , vol.%) in H_2O/CH_3CN mixtures [56].

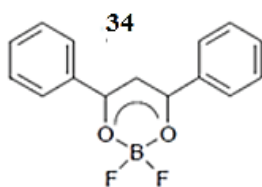
These three compounds have absorption bands with maxima in the near-UV region at 343 nm (**25**), 322 nm (**26**), and 386 nm (**24**). Weak emission with maxima at $\lambda_{fl} = 462$ and 423 nm and low quantum yields 0.0123 and 0.0134 is seen upon the photoexcitation of dilute solutions of **25** and **26** in THF, respectively. The emission maximum of **24** is even more strongly shifted toward the red region ($\lambda_{fl} = 527$ nm), while the fluorescence quantum yield is 0.0028. Thus, **25**, **26**, and **24** are extremely weak emitters when dissolved as individual molecules. The peripheral rings in **25**, **26**, and **24** can rotate in solution, rapidly losing excited state energy, which accounts for their low fluorescence quantum yields. When a large amount of water, in which these luminophores are insoluble, is added to solutions of **25**, **26**, and **24** in acetonitrile, their emission increases with increasing water content. In the solid state, **25** emits at $\lambda_{fl} = 478$ nm ($\phi = 0.68$), the emission maximum of **26** is at $\lambda_{fl} = 469$ nm ($\phi = 0.1$), while the fluorescence band of **24** is at $\lambda_{fl} = 532$ nm ($\phi = 0.33$).

Zhang et al. [57, 58] studied a series of AIE-active dyes, hexaphenyl-1,3-butadienes (**28-33**). The fluorescence intensity of these compounds in solutions with water content less than 60% in THF is negligible, which is attributed to nonradiative deactivation of excitation due to free intramolecular rotation about the σ -bonds between the phenyl and alkenyl groups.



The emission intensity sharply increases at water fraction up to 70%, which corresponds to the formation of aggregates of **28**, **29**, and **30** with mean particle diameter 330, 303, and 234 nm, respectively [57]. Aggregates of **31** (mean particle diameter 64-67 nm), **32** (144 nm), and **33** (125 nm) are formed when the water fraction is 90% [58]. The aggregates in H₂O/THF mixture are in an amorphous state and/or exist as a mixture of amorphous and crystalline formations. The emission quantum yields of **28** in the crystalline and amorphous states are 0.0353 and 0.0242, respectively. This indicates that the more compact crystalline aggregates are better luminophores. The quantum yield in the solid state for **31** $\phi = 6.74\%$ ($\lambda_{max} = 553$ nm), **32** - $\phi = 7.24\%$ ($\lambda_{max} = 510$ nm), and **33** - $\phi = 5.57\%$ ($\lambda_{max} = 537$ nm) [58]. The fluorescence increases sharply with increasing water content up to 90% in H₂O/THF: by factors of 14, 12, and 17 for **28**, **29**, and **30**, respectively, by a factor of 50 for **31** and by a factor of 7 for **32**.

For difluoroborate derivative with a dibenzoylmethane fragment (**34**) in a matrix of PMMA, the capacity to produce AIE was established by measuring the



changes in the monomer form of **34** upon the addition of water to its solution in acetone [59, 60]. The extent of aggregation of the luminophore increases in the presence of water. The intensity of the monomer fluorescence with maximum at 420 nm increases in the first stage of this process. The greater aggregation is

manifest also in the lifetime of the excited state of **34** from 0.5 to 2.4 ns.

The emission lifetime of the excited monomer form of **34** in the polymer matrix is somewhat greater (0.61 ns) in comparison with solution, which is attributed to a

decrease in the probability of nonradiative processes. The longer-lived emission, whose contribution increases with increasing recording wavelength, is related to the luminescence of excimers. Still another process with $\tau = 3.5$ ns and $\lambda_{fl} = 445$ nm is attributed to AIE [59, 60].

Nanoparticles of 6,7-dimethyl-2,3-di(4-(2,3,4,5-tetraphenyl)phenyl)quinoxaline (**35**), which is a polyphenylphenyldendron, display sensitivity toward nucleic bases in aqueous solutions and are hence used to determine these bases [61].

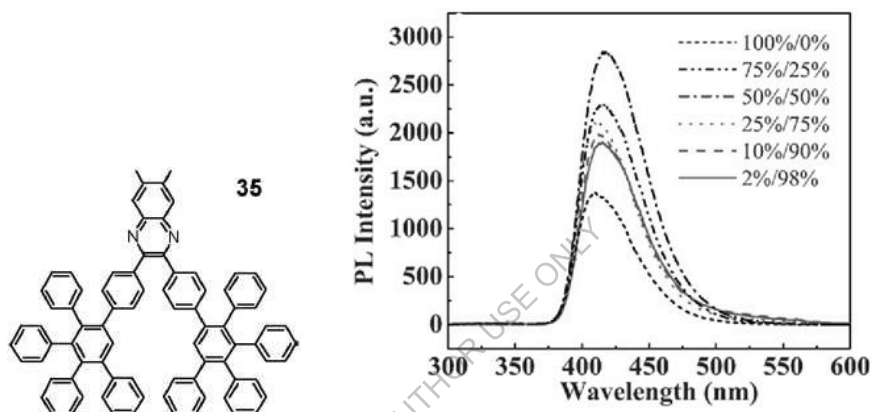


Fig. 7. Fluorescence spectra of **35** in THF/H₂O mixtures with component ratios (%) ($\lambda_{exc} = 280$ nm, $C = 9 \cdot 10^{-6}$ M). Reprinted with permission [61]. Copyright ©2008. The Royal Society of Chemistry.

Derivative **35** fluoresces in THF with maximum at 412 nm. In contrast to many AIE luminogens, the emission of **35** in THF/H₂O mixture does not change with increasing concentrations of this compound in solution. This finding may be the result of a combination of effects: intramolecular rotation, intermolecular hydrogen bonding, solvent viscosity, and hydration. Furthermore, the formation of nanoparticles of **35** with mean diameter 165 nm is observed in aqueous solutions. Due to the aggregation of **35** in THF/H₂O mixtures, when the water fraction increases from 0 to 50%, restriction of the intramolecular rotation in these molecules leads to a two-fold increase in the emission and a slight shift in the emission maximum toward the red region by 4-6 nm ($\lambda_{fl} = 420$ nm) (Fig. 7).

Rajagopal et al. studied the effect of the acylation [62] and benzoylation [63] of pyrene (P) on the crystal structure of **36-39**. The acylation of pyrene is accompanied by a considerable decrease in the interplane angle between adjacent units in the crystal of **36** ($\theta = 48.4^\circ$) and **39** ($\theta = 0^\circ$). Decrease in the interplanar angle was accompanied by transformation of the herringbone structure of **36** to the columnar structure of **39** (Fig. 8).

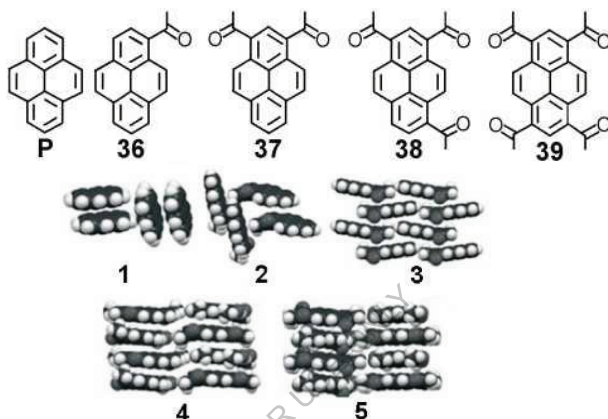


Fig. 8. Structures of aggregates of pyrene and its derivatives **36-39** in the crystalline state: pyrene (1, sandwich-herringbone structure, $\rho = 3.40$); **33** (2, herringbone structure, $\rho = 19.54$); **37** (3, lamellar π - π -stacking structure, $\rho = 2.56$); **38** (4, columnar π - π -stacking structure, $\rho = 0.89$); **39** (5, columnar π - π -stacking structure, $\rho = 0.46$) (ρ is the contribution of C-H and C-C interactions in the crystal, %). Reprinted with permission [62]. Copyright © 2014, The Royal Society of Chemistry.

An increase in the number of acetyl groups in chloroform solution leads to a bathochromic shift of the absorption maximum of **36-39**, in particular, by 22 nm for **36** ($\lambda_{\text{abs}} = 359$ nm) and by 70 nm for **39** ($\lambda_{\text{abs}} = 407$ nm) relative to the absorption of pyrene ($\lambda_{\text{abs}} = 337$ nm). The emission maxima of its acyl derivatives in this solvent also undergo a bathochromic shift with a significant decrease in the fluorescence quantum yield: $\lambda_{\text{fl}} = 412$ nm, $\phi = 0.004$ for **36** and $\lambda_{\text{fl}} = 435, 535$ nm, $\phi = 0.002$ relative to the emission of P ($\lambda_{\text{fl}} = 393$ nm, $\phi = 0.75$).

Derivatives **36-39** in the crystalline state all display a red shift in their spectra

relative to the position of the absorption bands and emission of pyrene $\lambda_{\text{abs}} = 386$ nm, $\lambda_{\text{fl}} = 472$ nm ($\phi = 0.67$). Thus, in the case of **39**, $\lambda_{\text{abs}} = 486$ nm and $\lambda_{\text{fl}} = 646$ nm ($\phi = 0.071$). The red shift of the excimer-like fluorescence structures of **36-39** was related to the combination of additional conjugation involving the acetyl groups and increased overlap between adjacent pyrene fragments. An enhanced fluorescence quantum yield in the crystalline state is observed for all derivatives **36-39**. The highest quantum yields found for **37** ($\phi = 0.325$) and **38** ($\phi = 0.277$) were related to the formation of J-aggregates [62].

Along with the acylation of pyrene, the benzylation of this compound also leads to the formation of luminescing green-yellow-orange crystals. AIE arises in **40-43** due to restriction of rotational motion of the benzoyl groups and the lack of solvation in the crystalline state, which is supported by the finding of greater fluorescence quantum yields of crystalline **40-43** ($\phi \approx 0.02-0.26$) than for solutions of these compounds ($\phi < 0.01$) (Fig. 9a). The benzoylpyrene derivatives have broad colored gamma emission, which is used in light emitting devices [63].

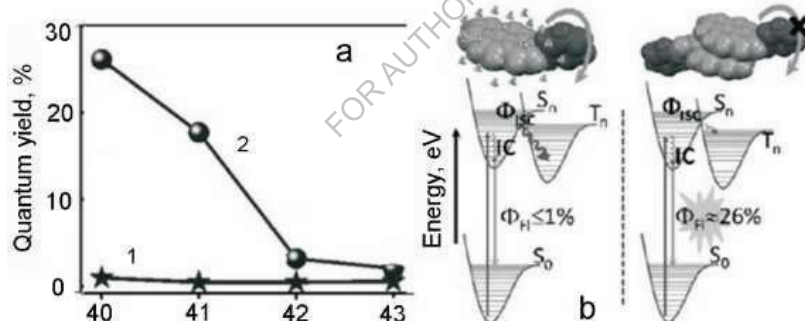
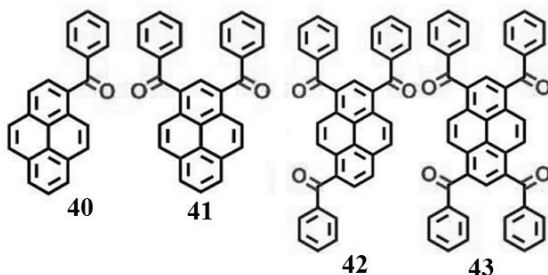


Fig. 9. a) Fluorescence quantum yield of **40-43** in solution (1) and in the crystalline state (2); b) Jablonski diagram representing the energy levels for **40** in solution (left) and the aggregate of **40** in the crystal (right). Reprinted with permission [63]. Copyright © 2016. The Royal Society of Chemistry.

An increase in the number of benzoyl groups leads to a red shift in the absorption spectra, for example, by 114 nm (**40**) and by 60 nm (**43**) in comparison with crystalline P. Upon excitation at 380 nm, **40** demonstrates a broad emission band

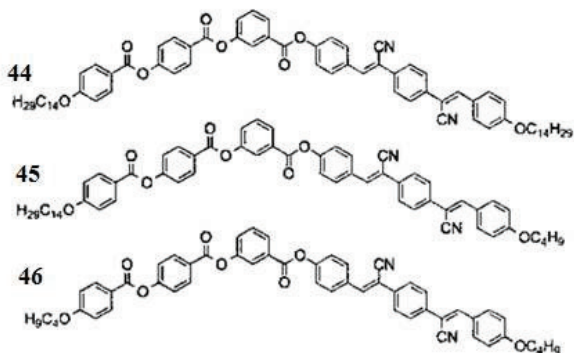
with maximum at $\lambda_{fl} = 620$ nm with a bathochromic shift of 148 nm relative to the emission maximum of crystalline pyrene.



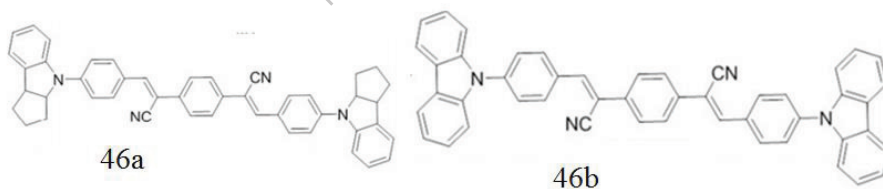
The increasing number of benzoyl groups in the series **41-43** is accompanied by a blue shift of the emission maximum relative to the emission spectrum of **40**. The observed differences in the position of the emission band maxima for **40-43** may be consequences of different extents of π - π -overlap and distance between the molecular planes of adjacent pyrene units. The difference in energies between the S_1 and T_1 states in the monomer and dimer of **40** is 1.18 and 0.94 eV, respectively. The low fluorescence quantum yield of solutions of **40** may be a consequence of efficient intersystem crossing (ISC) due to strong mixing of almost degenerate singlet and triplet states (Fig. 9b).

The spectra of dilute solutions of the twisted structures of dicyanodistyrylbenzene derivatives **44**, **45**, and **46** with various terminal alkoxy substituents (*para*-tetradecyloxy or *para*-butoxy groups) in dichloromethane (DCM) show absorption bands at about 270 and 372 nm due to the polybenzoate and distyryl chromophores as well as a weak luminescence band with maximum $\lambda_{fl} = 455$ nm ($\phi = 0.002$).

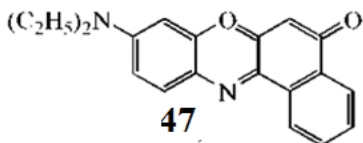
The emission maxima of solid solutions of these compounds in PMMA films are shifted toward the blue region to 440 nm, while the emission quantum yield rises to $\phi = 0.04$. The emission bands of powders of **44**, **45**, and **46** are found at longer wavelengths ($\lambda_{fl} = 573$ -588 nm) in comparison with solution.



Martinez-Abadia et al. [33] reported that the quantum yields of the powders are higher than in solution (DCM) and similar to the emission yields of solid solutions in PMMA ($\phi = 0.04\text{-}0.06$). However, considering the values given for nonradiative degradation rate ($6.6 \cdot 10^{-7}$ s) and radiation velocity ($4.2 \cdot 10^{-6}$ s), the emission quantum yield of the powders is 0.88. Such effects are also characteristic for α -cyanostilbenes and have been attributed to the effect of the viscosity of the medium, which hinders nonradiative deactivation involving rotation. Molecules of similar donor-acceptor structure **46a** and **46b** have emission characteristics typical for induced aggregation (high quantum yield in solid state and lack of fluorescence in solution) [64].



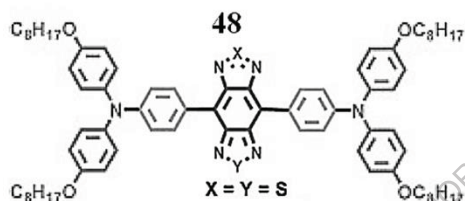
Rotation about the C-N Bond. The effect of enhanced emission in the solid state due to restriction of intramolecular rotation about the C-N bond is characteristic for Nile red (**47**), which is one of the best known highly fluorescent dyes with pronounced solvatofluorochromic properties (the quantum yield of **47** varies from 0.57 in ethanol to ~ 0.7 in other solvents). Strong quenching of the emission of **47** ($\phi =$



0.018) is observed in media containing water [65].

In order to study the AIE effect, nanoparticles of **47** were encapsulated in pure silica obtained by the hydrolysis of tetramethylorthosilicate and into hybrid sol-gel matrices obtained from glycidoxypropyltrimethoxysilane. When the concentration of **47** increase from $3 \cdot 10^{-5}$ to $1.5 \cdot 10^{-3}$ mmol/l in the silica samples it leads to the formation of nonfluorescing sandwich-type aggregates and an increase in the fluorescence intensity is noted in the hybrid glasses by a factor of 525 in comparison with the emission of **47** in SiO_2 matrices [66].

The luminophore 4,8-bis[4-(N,N-bis(4-octyloxyphenyl)amino)phenyl]1,2-c:4,5-c']bis([1,2,5]thiadiazole) (**48**) in the solid state shows an AIE effect in the near-



IR spectral region ($\lambda_{fl} = 1078$ nm) (Fig. 10a) [67]. The absorption and luminescence maxima of **48** in toluene are at $\lambda_{abs} = 763$ nm and $\lambda_{fl} = 1065$ nm; the emission quantum yield $\phi = 0.071$.

Upon the addition of methanol (up to 70 vol%) to a solution of **48** in THF, the fluorescence quantum yield ($\phi \approx 0.001$) remains virtually invariant and then rises sharply to $\phi \approx 0.29$ at methanol concentration 90 vol % in the solvent mixture (Fig. 10b). Qian et al. [67] suggested that the origin of the AIE effect in dye **48** is related to a mechanism of restriction of intramolecular vibrational and rotational motions in the solid state.

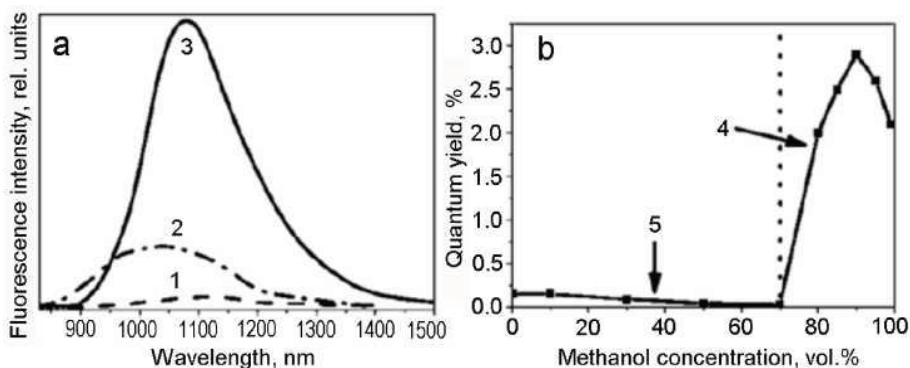


Fig. 10. a) Fluorescence spectra of **48** in THF solution (1), in THF/ CH_3OH (1:9 vol.) mixture (2),

and in a film (3) ($C = 10 \mu\text{M}$, $\lambda_{\text{exc}} = 700 \text{ nm}$ (for solution), 694 nm (for film)); b) dependence of the quantum yield of **48** on the composition of the THF/ CH_3OH mixture: 5 - isolated particles and 6 - nanoscopic aggregates. Reprinted with permission [67]. Copyright © 2008, American Chemical Society.

Rotation about the N-N Bond. An AIE effect is observed in a series of salicylaldehyde azines [68], in which the salicylaldehyde parts are attached to each other by means of an N-N single bond. Intramolecular hydrogen bonds permit rotation only about the N-N bond. Solutions of 4-hydroxysalicylaldehyde azine (**49**), salicyl aldehyde azine (**50**), and 5-chlorosalicyl aldehyde azine (**51**) in 9:1 ethanol/water have structured bands in their absorption spectra and weak fluorescence. Enhanced intensity of the absorption band in the long-wavelength spectral region and the appearance of fluorescence are observed in 1:9 ethanol/water (Fig. 11). Increased luminescence of these compounds was also found in a viscous glycol/glycerin solvent. The emission quantum yields of **49-51** in solution are 0.002, 0.002, and 0.001, respectively, while these values in the aggregated state are 0.13 ($\tau = 3.09 \text{ ns}$), 0.11 ($\tau = 3.05 \text{ ns}$), and 0.05 ($\tau = 2.32 \text{ ns}$), respectively.

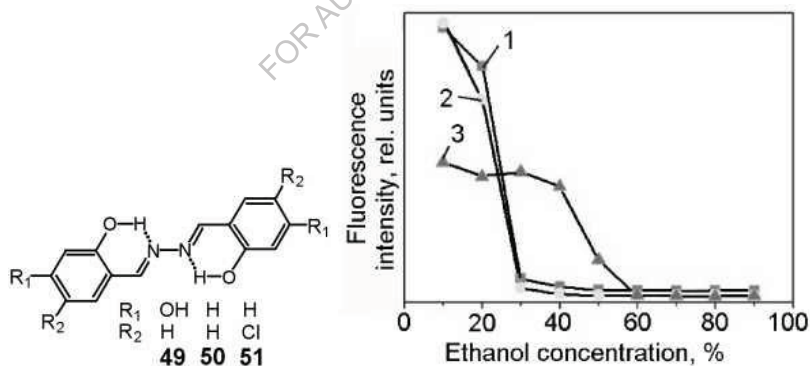


Fig. 11. Effect of the volumetric fraction of ethanol on the fluorescence intensity of azine derivatives **49** (1), **50** (2), and **51** (3) in ethanol/water mixture ($\lambda_{\text{exc}} = 400 \text{ nm}$). Reprinted with permission [68]. Copyright © 2009, American Chemical Society.

Figure 11 shows that the onset of the AIE effect is seen at 30 vol.% ethanol for **49** and **50** and 60 vol.% for **51**. Salicyl aldehyde azine (**50**), which is a symmetrical

Schiff-base, has weak emission ($\phi = 0.002$) in ethanol solution but its luminescence increases upon the addition of water, which facilitates the formation of aggregates. Tang et al. [68] assumed that the hydroxyl groups of the ethanol solvent molecules compete with the hydroxyl groups of **50** in the formation of intermolecular hydrogen bonds, which is not quite in accord with the proposed mechanism since there are also hydroxyl groups in water molecules and intermolecular hydroxyl groups may be formed with **50**.

AIE properties are also characteristic for 2-(1-hydroxy-2-naphthyl)methylenehydrazone (**52**). The luminescence intensity of this compound increases significantly upon the addition of water to its solution in DMF (Fig. 12). The emission quantum yields of **52** in pure DMF and in the aggregated state are 0.057 and 0.27, respectively [69].

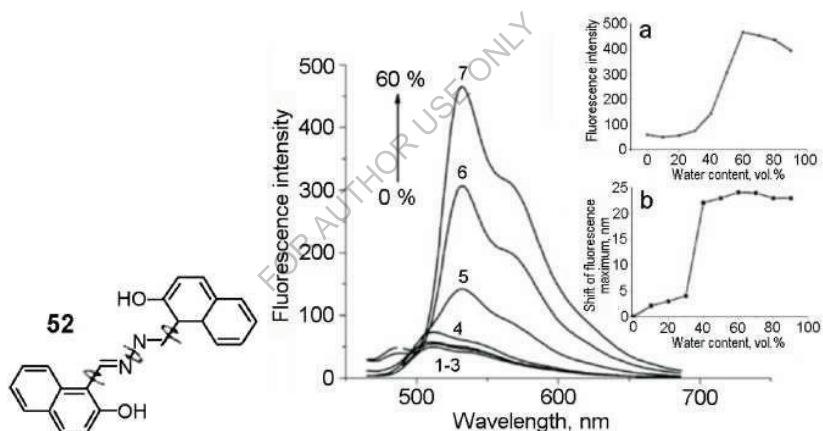
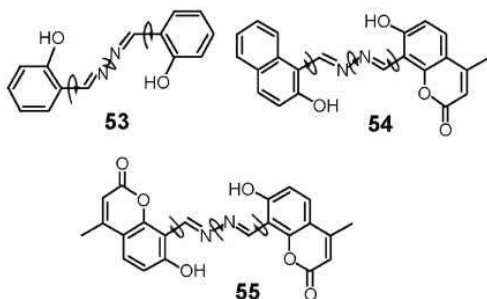


Fig. 12. Change in the fluorescence intensity of **52** with increasing water fraction in DMF/H₂O mixture: 1) 0, 2) 10, 3) 20, 4) 30, 5) 40, 6) 50, 7) 60 vol.%. Inserts: a) change in the integral fluorescence intensity of **52** with increasing water content in DMF/H₂O mixture; b) change in the position of the fluorescence maximum of **52** with increasing water content. Reprinted with permission [69]. Copyright © 2013, Elsevier.

The AIE effect is also characteristic for azines **53-55**, which contain various groups, including 4-coumarin, in which intramolecular proton transfer is possible in the excited state [70]. The emission quantum yields of these compounds in the

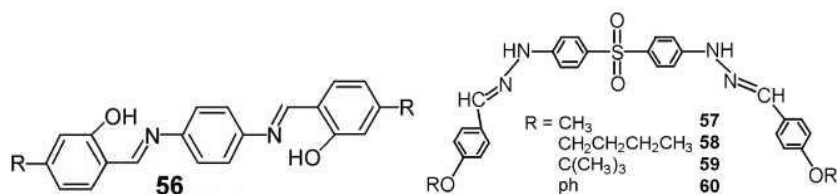
aggregate state are 0.55 and 0.83, respectively, while their solutions in DMSO hardly fluoresce. In the isolated state, the mobile units in these luminogen molecules rotate



about the C-C and N-N bonds of the enol-form or the C-C, N-N, and C-N bonds of the keto-form, quenching the energy of the excited state and facilitating nonradiative relaxation.

The molecules “freeze up” in the aggregate or solid state, which hinders intramolecular motion thereby facilitating radiative deactivation of photoexcitation. Thus, the introduction of various groups from phenyl and naphthyl groups to the 4-methylcoumarin group permits us to alter the luminescence color of the resultant luminophores from green (**53**) to yellow (**52**), orange (**54**), or red (**55**).

Derivatives of *N, N'*-bis(salicylidene)-*p*-phenyldenediamine (**56**) also display AIE. These compounds have weak luminescence in THF, but strongly emit upon aggregation in THF/H₂O mixture with 90 vol.% water. The emission quantum yield of these compounds in THF/H₂O mixture with 90 vol.% water ($\lambda_{\text{exc}} = 360$ nm) is 0.33 for R= H (**9**), 0.08 for R = Me (**56**), and 0.12 for R = OMe (**56**), which is greater than in pure THF by factors of 400, 80, and 18, respectively [71].



Similar changes in spectral-luminescent properties in going from solutions in pure THF to THF/H₂O mixture were found for the series of *bis*-4,4'-di(E)-2-(4-4-alkoxyaniline)hydrazinyldiphenyl sulfones (D- π -A- π -D) [72]. The emission quantum yields of these compounds in THF/H₂O mixture are greater than in THF solution; the enhancement is from 0.004 to 0.027 for R = CH₃ (**57**), from 0.003 to 0.069 for R = CH₂-CH₂-CH₂-CH₃ (**58**), from 0.0003 to 0.057 for R= C(CH₃)₃ (**59**), and from 0.0016

to 0.22 for R = Ph. The formation of aggregates due to intermolecular hydrogen bonding between adjacent molecules, which hinders intramolecular rotation, leads to enhancement of AIE.

2.2. Restriction of Intramolecular Vibrations

Studies of AIE-luminophores have shown that some of these molecules lack rotating fragments. Thus, the appearance of AIE for such molecules cannot be explained by the RIR mechanism but may be described satisfactorily by the RIV mechanism. Examples of such compounds are 10,10',11,11'-tetrahydro-5,5'-bidibenzo[a,d][7]annulenyliidene (**61**) and 5,5'-bidibenzo[a,d][7]annulenyliidene (**62**) [73]. The emission peak in the longer wavelength region (395 nm) with quantum yield 0.3 could be observed. Solutions of these compounds have very weak emission with quantum yield 0.001 and 0.005, respectively.

The results of computer modelling carried out using the hybrid QM/MM method combining molecular mechanics and quantum mechanics procedures showed that an isolated molecule of **61** has six normal vibrational modes, which consume a considerable amount of excited state energy (the reorganization energy of each mode $>200\text{ cm}^{-1}$, which leads to a total energy loss of 5679 cm^{-1}).

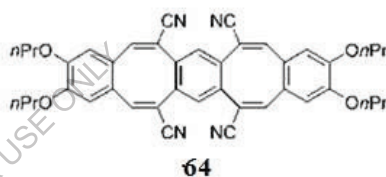
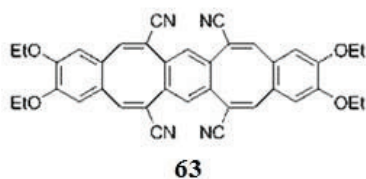


For comparison, **61** in a cluster have only three normal modes, which consume a much smaller amount of excitation energy ($\sim 4016\text{ cm}^{-1}$). In this case, the combination of a reduced number of normal vibrational modes and the loss of $\sim 30\%$ of the exciton energy due to intramolecular vibrations permits deactivation of the excited state of **61** through a radiative channel, which leads to the observed AIE effect [73,74].

The RIV mechanism responsible for the AIE effect has been proposed in a study of a series of π -systems containing flexible cyclooctatetraene (COT) rings [75]. Conformational changes of the COT rings in these molecules permit structural flexibility. In solution, these compounds may undergo various vibrational inversions,

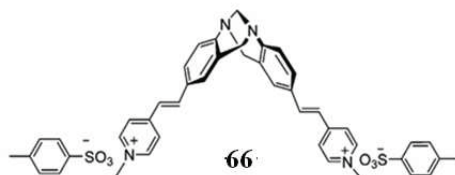
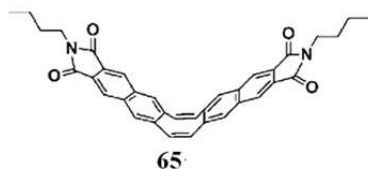
leading to the formation of boat-boat, boat-chair, and chair-chair conformations.

Such intramolecular vibrations lead to nonradiative loss of excitation energy as a result the solutions of these compounds do not fluoresce. In the crystalline state, conformational changes of the COT rings are hindered by intermolecular interactions and steric packing effects, hindering intramolecular vibrations. The nonplanar molecular structure also hinders intermolecular π - π stacking interactions. Together these effects lead to the appearance of luminescence in crystals of these compounds. Although they fluoresce only weakly, their solvated monocrystals emit at 450-500 nm. The emission quantum yields of **63** in CHCl_3 , **64** in CH_2Cl_2 , and **64** are 0.038, 0.06, and 0.071, respectively, which is greater than in their solutions by factors of 380, 600, and 710, respectively



Derivatives **63** and **64** form powders in the solid state, which have very weak emission due to vibration of the COT ring.

Molecules consisting of a flexible COT ring connecting two N-arylimide groups through phenyl, naphthyl (**65**), and anthracene units are also AIE-luminogens [76], as indicated by the lack of emission in solutions and the appearance of strong fluorescence in the aggregate state at a band with maximum 412 nm with quantum yield 0.17.

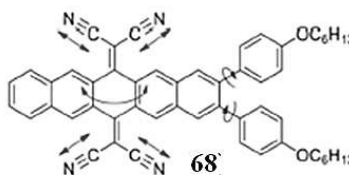
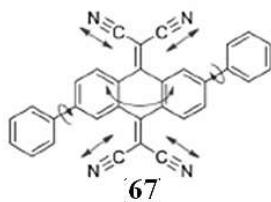


Enhancement of fluorescence intensity is also observed upon cooling a solution of **65** in 2-methyltetrahydrofuran from 296 to 103K with a hypsochromic shift of the

emission maximum to 393 nm. Another flexible molecule, 2,8-(6H,12H-5,11-methanodibenzo[b,f]diazacinylidene)-di(*p*-ethenyl-*N*-methylpyridinium)ditosylate (**66**) is also a typical AIE luminogen [77]. Ditosylate (**66**) consists of a V-shaped unit with styrylpyridinium blocks on each side, which are reminiscent of stilbene structure. The fluorescence spectrum of **66** extends to 510 nm and has a maximum at 400 nm, while a band with maximum at $\lambda_{fl} = 550$ nm is observed in acetonitrile-toluene. The intensity of this band increases by a factor of 225 with increasing toluene fraction up to 98% due to the formation of aggregates.

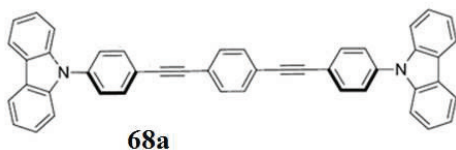
2.3. Restriction of Intramolecular Motion

This mechanism is used to explain the AIE effect in compounds, in which it is impossible to distinguish between rotational and vibrational motions. An example is 11,11,12,12-tetracyano-(2,6-diphenyl)-9,10-anthraquinodimethane (**67**), in which the central unit is connected to two phenyl rings at C-2 and C-6. This compound does not luminesce in acetonitrile and upon the addition of a small amount of water. Enhanced emission by a factor of 33 is observed when the water content exceeds 60% [78].



Tetracyano derivative **68**, in which the pentacenequinodimethane unit is attached to identical phenyl groups, is a structure also possessing AIE luminogen properties. This compound does not fluoresce in THF solution but emits in THF/H₂O mixture with water content about 70 vol.%, which favors the formation of fluorescent nanoaggregates [79, 80].

The low luminescence quantum yield of a solution of 1,4-bis(((9H-carbazol-9-yl)phenyl)ethynyl)benzene (**68a**) in THF is attributed to very rapid motions,

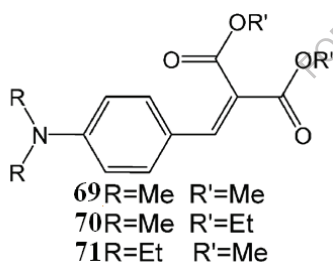


including rotation and/or vibration of several molecular fragments, which facilitates efficient nonradiative excitation energy degradation.

On the other hand, crystallization of this derivative decreases the frequency of molecular motions, leading to the enhanced emission in the solid state [81].

4-Dialkylamino-2-benzylidenemalonic acid esters **69-71** in dilute toluene have hardly detectable emission ($\phi \approx 0.001$) at $\lambda_{fl} = 429$ nm (**69**) and $\lambda_{fl} = 440$ nm (**70**) [82], but fluoresce with higher quantum yields up to $\phi \approx 0.38$ as powders. A significant red shift of the emission bands to 468 and 473 nm is observed. A significant increase in the quantum yield of **69** from 0.001 in THF to 0.026 in more viscous solvent, such as, polyethylene glycol was noted. Enhanced emission is also observed when water is added to solution of **69** in methanol at water content above 50 vol.%, which leads to aggregation of molecules with pseudonanostructures formation and stronger luminescence.

Crystalline films of **69** have bright blue emission with maximum at $\lambda_{fl} = 468$ nm and quantum yield 0.38. In contrast, its amorphous films demonstrate only weak blue-green fluorescence ($\lambda_{fl} = 500$ nm) at room temperature with quantum yield 0.01.



The lowest quantum yield ($\phi \approx 0.003$) was found for **69** in PMMA. We should note that the fluorescence intensity is significantly higher with decreasing temperature of a solution of **69** and upon cooling a PMMA film containing **69** [82].

The weak fluorescence of solution **69** in methanol and stronger emission in the crystal are in accord with the results of TD-DFT, CASSCF, and ONIOM (QM : MM) quantum chemical calculations [83].

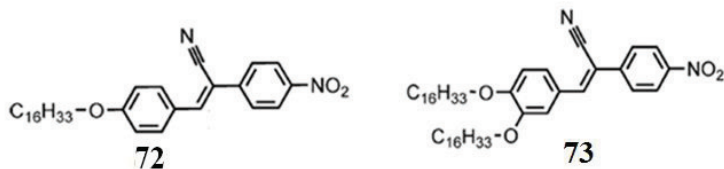
3. Fluorescent Properties of Aggregates of J-Type Molecules

An explanation of molecular packing effects on the photophysical properties of aggregates was proposed more than five decades ago by M. Kasha [84], who showed that the coulombic interaction between two molecules induces spectral shifts of the

absorption bands and leads to change in the radiative degradation of the excitation of such molecules in comparison with the free molecules. In J-aggregates, dipole moments line up from head to tail, which leads to a bathochromic shift of the absorption bands and enhancement of the rate of radiative degradation of excitation energy [84]. J-Aggregates are building blocks in the formation of nanoparticles and thus determine the efficiency of their fluorescence [35, 85-87]. J-Aggregates, in which molecules are arranged head-to-tail, specifically tend to have relatively high fluorescence efficiency [88, 89]. The authors of studies [85, 90-92] have assumed that the structure of organic compounds crystals consisting of J-aggregates determines their photooptical properties.

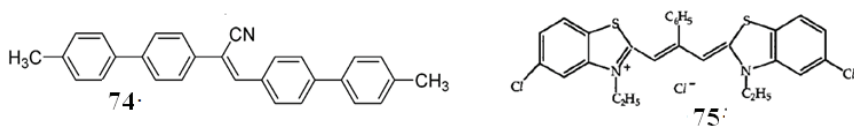
Shapiro et al. [93] studied meso-alkyl-substituted thiocarbocyanine dyes and found that the ethyl group, as a rule, facilitates the formation of J-aggregates in aqueous solution, while the methyl group facilitates the formation of various types of H^{*}-aggregates. The introduction of the multicharged Eu⁺³ cation into aqueous solutions of these dyes shifts the equilibrium toward aggregates: the meso-CH₃-substituted dyes form mostly H^{*}-aggregates, while meso-C₂H₅-substituted dyes form mostly J-aggregates. Thus, the alkyl group in the meso-position relative to the polymethine chain in thiocarbocyanines acts as a regulator in the aggregation process due to stereochemical effects and dictates the morphology and spectral properties of the resultant aggregate [93].

Examples of compounds displaying enhanced fluorescence due to the formation of J-aggregates during the sol-gel phase transformation are (Z)-3-(4-hexadecyloxy)phenyl)-2-(4-nitrophenyl)acrylonitrile (**72**) and (Z)-3-(3,4-bis(hexadecyloxy)phenyl)-2-(4-nitrophenyl)acrylonitrile (**73**) [30], which fluoresce in pure THF with quantum yield ~ 0.005. Both compounds gelatinize in THF/H₂O mixture and in DMSO, while **73** form a gel upon ultrasonic treatment also in acetone with enhancement of the fluorescence by a factor of 70.



A significant increase in the emission intensity of these compounds was also observed upon decreasing the temperature. Thus, a hypsochromic shift of the emission maximum from 550 to 525 nm and a 20-fold increase in emission intensity is observed upon cooling a solution of **72** in DMSO from 100 °C to room temperature. The fluorescence of a solution of **72** in THF/H₂O at 60 °C is very weak. Upon cooling solution, the fluorescence maximum shifts from 535 to 525 nm and its intensity increases by a factor of 40 in comparison with the hot solution in THF/H₂O and a factor of 90 relative to a solution of the same concentration in pure THF. The weak emission band at $\lambda_{fl} = 540$ nm for **73** in THF/H₂O at 60 °C bathochromic shifts to 574 nm upon cooling the solution to room temperature, which is accompanied by a seven-fold increase in the emission intensity.

An effect of aggregation on emission is also observed for cyanostilbenes [31], which are linear π -conjugated organic luminophores. The authors of study [17] attributed the changes in the spectral-luminescent properties of 1-cyano-trans-1,2-bis(4'-methylbiphenyl)ethylene (**74**) to intra- and intermolecular interactions. Isolated molecules of **74** in THF/H₂O mixture with water content up to 50% hardly fluoresce ($\phi \approx 0.001$). The emission quantum yield is enhanced when there is 60 vol.% water in the solvent mixtures and spherical nanoparticles of **74** begin to form with mean diameter 30-40 nm.

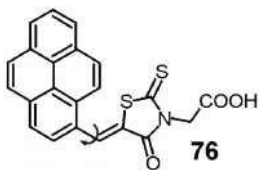


When the water content is 80%, the fluorescence quantum yield is enhanced by a factor of almost 700 ($\phi = 0.69$) relative to the emission quantum yield of **74** in pure THF and there is a bathochromic shift of the emission band from $\lambda_{fl} = 455$ nm to $\lambda_{fl} =$

488 nm. The enhancement of the fluorescence of nanoparticles of **74** is attributed to the synergistic effect of planarization and J-aggregation [94]. Semi-empirical AM1 calculations supported the hypothesis that aggregation facilitates flattening the plane of molecules of **74**, favors expansion of the effective length of the conjugation chain, and enhances the oscillator strength of this molecule.

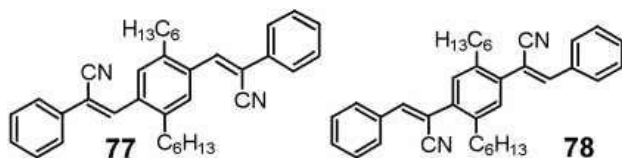
Enhancement of emission when the formation of J-aggregates is possible was observed in a study of the properties of 3,3'-diethyl-5,5'-dichloro-9-phenylthiacarbocyanine (**75**) [95]. The absorption spectra of **75** in methanol have bands with maxima at 528 and 566 nm and emission band at 582 nm with emission quantum yield $\phi \approx 0.015$. The addition of aqueous KCl to solution of this dye in methanol, i.e., when conditions are created for the formation of J-aggregates, the absorption spectrum retains the monomer band at 566 nm, but a new band appears at 673 nm related to absorption of the J-aggregate of **75**. The emission spectrum also has two bands: a band at 673 nm related to the J-aggregates and a band at 578 nm, which corresponds to monomer forms of the fluorophore. The fluorescence quantum yield of the monomer taken in aqueous solution as unity is 0.015 in methanol. Upon excitation at $\lambda = 575$ nm, the quantum yield is increased by a factor of 10, while upon excitation at $\lambda = 615$ nm, the yield is enhanced by a factor of 22.

An AIE effect has been described for a pyrene derivative of rhodaninacetic acid (**76**), which is an organic donor-acceptor compound capable of forming particles with mean diameter 50-60 nm with strong red emission [96]. The absorption spectrum of **76** in methanol has a band at 333 nm typical for pyrenes and a charge transfer band at 442 nm. The charge transfer band is shifted to 502 nm upon the addition of water to solution of **76** in methanol, which is ascribed to greater effective length of the conjugation chain due to planarization of the molecule induced by aggregation, along with the appearance of a shoulder at 531 nm attributed to the formation of J-aggregates. The fluorescence spectrum of **76** in methanol has a band at 542 nm, which a bathochromic shifts to 628 nm ($\Delta\lambda = 86$ nm) in water-methanol (9:1) mixture due to the nanoparticles formation.



Quantitative evaluation of the ratio of the fluorescence intensities of solutions in methanol and water-methanol showed that the emission intensity of the mixed solution increases by a factor of 4-40 with increasing water volumetric fraction to 70%-90%. The luminescence quantum yield of solution of **76** in methanol is extremely low $\phi = 0.004$. But increasing the water content to 90 vol.%, leads to nanoparticles formation, and enhancement of $\phi = 0.180$ [96].

Benzene derivatives 1,4-bis(α' -cyanostyryl)-2,5-di-*para*-hexylbenzene (**77**) and



1,4-bis(β -cyanostyryl)-2,5-di-*para*-hexylbenzene (**78**) are clear examples of rod-like π -conjugated molecules, which form a family of phenylenevinylene derivatives [34]. Most of these compounds fluoresce in solution with high quantum yield close to unity [97]. Oligophenylenevinylenes with electron-donor and/or electron-acceptors substituents are precipitated from the vapor phase and solution as ultrathin films or nanoparticles with diameter 20-200 nm. The fluorescence quantum yield of the starting oligomers and their alkyl or oxyalkyl derivatives have high quantum yields in solution $\phi \approx 0.5$. The value of the quantum yield drops sharply in films and nanoparticles due to the formation of H-aggregates. However, the emission quantum yield may be raised to ~ 0.7 by the introduction of fluorescent acceptors. Furthermore, the quantum yield can also be raised to ~ 0.6 by increasing the medium viscosity, which hinders torsional rotation of the molecular fragments and blocks the transition of the molecules to the twisted intramolecular charge transfer (TICT) state, or upon transition of **77** and **78** to the solid state due to the formation of J-aggregates with a high emission rate constant k_f . That is characteristic both for **77** possessing extremely weak fluorescence in liquid solutions ($\phi \approx 2 \cdot 10^{-3}$) and high quantum yield in the aggregate state or films ($\phi \approx 0.6$) and for **78**.

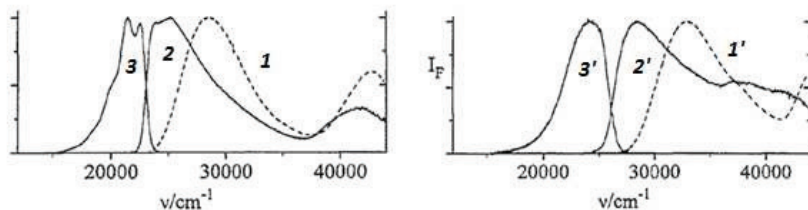
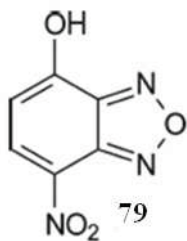


Fig. 13. Absorption spectra of solutions in dichloromethane (1, 1'), fluorescence excitation spectra (2, 2'), and fluorescence spectra (3, 3') of nanoaggregates or microcrystals of **77** (1, 2, 3) and **78** (1', 2', 3'). Reprinted with permission [34]. Copyright © 1996, Elsevier

Quenching of luminescence in these compounds is mainly due to steric factors caused by a strong deviation from planarity, which increases the rotation-induced non-radiative deactivation. The luminescence bands of **77** and **78** are strongly shifted relative to their bands in the absorption spectra, which indicate a less twisted conformation in the S_1 state (Fig.13) [34, 98].

4. Luminescence of Pairs of Organic Ions and Transition Metal Complexes

An example of AIE pairs of organic ions caused by the aggregation was presented by Lamere et al. [99]. The anionic form of 4-hydroxy-7-nitrobenzoxadiazole (**79**), NBDO^- , which readily forms a salt with the organic cation in tetrabutylammonium bromide (TBAB), served as the fluorescing fragment. The absorption spectrum of undissociated **79** has medium-intensity bands with maxima at 382 and 394 nm, whose position depends on the nature of the solvent. In chloroform, this compound emits at 554 nm very weakly ($\phi = 2 \cdot 10^{-3}$).



The UV absorption spectra of TBAB+ NBDO^- in various solvents are very similar to the spectrum of the NBDO^- ion arising due to dissociation of **79** in water at pH 5.0. The absorption spectra have charge transfer bands with maxima at 461 and 468 nm, whose intensity is 3-fold higher than for undissociated **79**. The emission spectrum is independent of the excitation wavelength, which supports the hypothesis of a single emission site. The emission spectrum has bands

with maxima at 538 and 586 nm. The quantum yield in all organic solvents is about 10^{-2} but about 10^{-3} in water. The low emission quantum yield of the NBDO⁻ anion in water may be attributed to the quenching of the excited state of NBDO⁻ by water molecules. Increased luminescence was observed in the presence of the salt TBAB/NBDO⁻ formed upon mixing solutions of **79** and TBAB. This increase is related to the formation of fluorescent microcrystals with length up to 60 μm .

Crystals of **79** have a weak luminescence band with maximum at 520 nm and quantum yield $6 \cdot 10^{-3}$, while the emission intensity of the TBAB/NBDO⁻ microcrystals is much higher. The emission has a band with maximum at 543 nm independently of the excitation wavelength with quantum yield $4.7 \cdot 10^{-2}$. Since the nature of the organic cation may be readily changed, such systems has great of interest for the development of new organic luminophores as micro- and nanoparticles, which should emit fluorescence in the solid state and, possibly, in aqueous media.

Little attention has been paid to the AIE of organometallic and coordination compounds as in experimentally studies as in theoretically. Phosphorescence is the predominant emission process for most transition metal complexes [100]. Induced aggregation phosphorescent emission (AIPE) has been found for a series of complexes with Re(I), Ir(III), Au(I), Zn(II), and Cu(I). As for organic compounds, the emission quantum yield of metal complexes is higher in poor solvents, in which highly-phosphorescing nanoaggregates are formed, which may serve as active components of bio- and chemosensors and optoelectronic devices [101].

Only a few iridium complexes with aggregation-induced phosphorescent emission (AIPE) have been studied extensively. Jiang et al. [102] studied the properties of electroneutral binuclear iridium (III) complex **80**, which displays AIPE. Shan et al. [103] have reported ionic mononuclear iridium (III) complex **81**, which also displays AIPE.

Binuclear complexes of iridium with diimine ligands (**82**, **83**), which can bind two metal sites, also hold potential for AIPE [104]. The electronic spectra of **82** and **83** have predominant absorption bands at 200-300 nm due to spin-resolved π - π^* -transitions of the ligands.

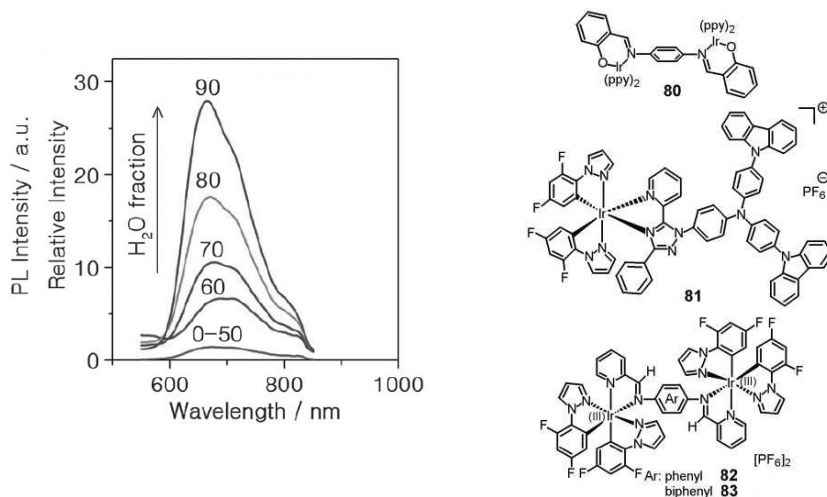
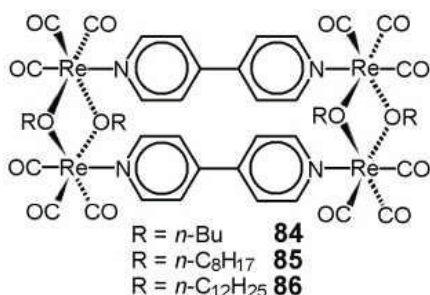


Fig. 14. Fluorescence spectra of **82** in $\text{CH}_3\text{CN}/\text{H}_2\text{O}$ mixture with different water content (vol.%) at room temperature. Reprinted with permission [104]. Copyright © 2014, The Royal Society of Chemistry.

The weak absorption at 350 nm is related to both metal-ligand and ligand-ligand charge transfer, which is characteristic for iridium (III) complexes. Complexes **82** and **83** hardly emit upon photoexcitation in acetonitrile solution but intense emit in the film at room temperature with $\lambda_{\text{em}} = 644$ and 692 nm, respectively. Thus, **83** is a long-wavelength emitting ionic complex of iridium (III). Complexes **82** (Fig. 14) and **83** in pure acetonitrile emit weakly, but when the water content in the mixed solvent is greater than 60 vol.%, the emission intensity is significantly enhanced. The quantum yields of **82** and **83** in a thin film are 0.37 and 0.26, respectively.

An AIE effect was also observed for rhenium-containing dyes (**84-86**) [105].



True solutions of these compounds do not emit but in moderate solvation media, they form luminescent supramolecular aggregates. Thus, the photoluminescence quantum yield of **86** in acetonitrile is only $\phi = 0.39 \cdot 10^{-3}$ but in

CH₃CN/H₂O mixture (1:9), quantum yield is seventeen-fold greater ($\phi = 6.54 \cdot 10^{-3}$) and the emission band maximum hypsochromic shifts from 666 to 602 nm.

5. APPLICATIONS OF AGGREGATION-INDUCED EMISSION

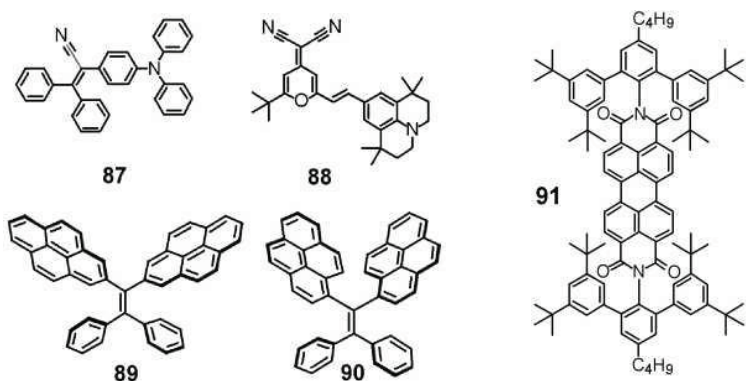
There has recently been exponential growth in theoretical and applied studies of AIE, which opens broad prospects for its practical use. From the viewpoint of designing new materials possessing AIE, there has been a tendency move away from the synthesis of simple AIE molecules to more functionalized structures, combining organic AIE luminogens with other organic and inorganic components or building blocks on the molecular and mesoscopic levels for the development of multifaceted luminogens such as metal organic frameworks derived from AIE luminogens and AIE metal complexes. The rational construction, especially of modular hybrid structures, may lead to advanced functional materials and systems with still greater potential for use in energy devices, environmental monitoring, biomedical investigations including the visualization *in vitro* and *in vivo* of biological structures such as organelles, cells, and tissues and the study of cell processes such as apoptosis and metastases.

5.1. Luminescent Solar Concentrators

First-generation dyes including coumarins, perylenes, and rhodamines used in luminescent solar concentrators (LSC) have a number of disadvantages, in particular, concentration and temperature quenching of luminescence, and small Stokes shifts, which lowers the efficiency of derived LSC [106]. Fluorophores displaying aggregation-induced emission are more promising materials for LSC [107-109]. Such compounds are less sensitive to fluorescence quenching at high concentrations, which facilitates efficient energy transfer in PMMA films [110].

These processes are seen, for example, using 2-(4-(diphenylamino)phenyl)-3,3-diphenylacrylonitrile (**87**), which displays AIE at high concentrations, as the energy donor and the highly-efficient luminophore of the dye 4-(dicyanomethylene)-

2-fer/-butyl-6-(1,1,7,7-tetramethyljulolidin-9-enyl)-4H-pyran (88) at low concentration as the acceptor.



LSC prepared using diphenylethenes of gem-pyrene (**89**, **90**) demonstrate high efficiency and a quantum yield in the amorphous and crystalline states: 0.14 and 0.39 for **89** and 0.39 and 0.55 for **90**, respectively [107]. LSC using a mixture of an isolated light absorber N,N-(2,6-bis(3,5-di-*tert*-butylphenyl)-4-butylphenyl)-perylene diimide **91**, which displays AIE, and perylene red (LR305) increase the efficiency of solar light conversion from 0.68 for individual perylene red to 0.72 for the mixture [111-113].

5.2. Optoelectronic Applications

AIE luminophores have now been synthesized with spectral emission encompassing the entire visible and even near-IR range with luminescence quantum yields in the solid state up to unity [114-116]. Such compounds have been used to create organic light diodes with both monochromatic red, green, and blue emission as well as white light emission [117, 118]. AIE compounds with delayed fluorescence consisting of carbazoly]- and phenothiazinyl]-substituted benzophenones are used for the manufacture of single-component AIE luminogens emitting white light. Such compounds demonstrate great potential for use in the development of simple and efficient devices for the emission of white light [119].

Another area of study, in which the AIE luminogens may be used, is in liquid

crystal displays [120]. Liquid crystals are non-emitting compounds and require backlighting for screen displays, complex design, and high energy consumption. Virtually any such display has an active matrix of transistors used to form the image, a layer of liquid crystals with light filters for selective light transmission, and a backlighting system, as a rule, consisting of light diodes. The latter is necessary for the display of color images. Liquid crystals derived from AIE systems give bright emission in the solid state, especially, in the highly-ordered crystalline state. Such substances provide a unique possibility of preparing light-emitting liquid crystal displays of simplified construction requiring lower energy consumption. Circularly-polarized luminescence (CPL) provides for the possibility of the transmission of stereochemical, conformational, and three-dimension-structural information, which is extremely necessary for 3D displays. In contrast to traditional materials of this type with a fluorescence quenching effect, AIE-active materials with CPL demonstrate intense fluorescence, strong circular dichroism signals, and high CPL dissymmetry coefficients in films, which have a great importance for further improvements of 3D displays [121].

5.3. Environmental Monitoring

The detection of ions of various compounds is one of the major problems in monitoring the environment since they play an important role in metabolism and biological systems. Coumarin and α -cyanostilbene were used to synthesize a selective and sensitive probe for the detection of Hg^{2+} ions based on the AIE effect. This probe weak fluorescence in solutions and enhanced emission in the solid state due to the formation of excimers and π - π stacking interaction of the coumarin groups [122].

Huerta-Aguilar et al. [123] described the fluorescence of a Schiff base, which can serve as a fluorescent probe, *N,N'*-propylene-*bis*(salicylimine) (salpn), for the detection of Al^{3+} ions with detection threshold $1.24 \cdot 10^{-3}$ mmol/L. Spherical fluorescent organic nanoparticles (FON) with diameter 100 nm acting as chemosensors have been obtain using salpn. The observed luminescence intensity enhancement of salpn FON in the presence of Al^{3+} ions may be ascribed to enhanced

fluorescence due to chelation of the receptor bound to Al^{3+} ions, which imparts rigidity to the system and the formation of J-aggregates.

Tetraphenylimidazole derivatives, which may form FON with AIE characteristics, were used to synthesize 2-(4-(1,4,5-triphenyl-1H-imidazol-2-yl)benzylidene)malononitrile (TIBM) for the selective detection of sulfites in the air, food products, and biological systems. This compound can assemble into well-organized nanoparticles with cetyltrimethylammonium bromide as a surfactant. The formed nanoparticles are the basis of nanosensor with a rapid response (15 s), high selectivity, and extremely low sulfite detection threshold (7.4 nM) in various media [124].

2-(2'-Hydroxyphenyl)benzimidazole (HPBI) is an active AIE fluorophore and demonstrated 4-fold greater emission upon aggregation in comparison with the aqueous solution. The penetration of the aggregated structures into living cells makes HPBI an efficient system for studying cell deformation since the monomers do not give any visible fluorescence within cells [125].

2-(*tert*-Yliminomethyl)quinolin-8-ol (HL), which displays an AIE effect, is a chemosensor for the detection of Zn^{2+} ions in a ZnL_2 complex with high selectivity and sensitivity in aqueous media. ZnL_2 also fluoresces in the solid state. The emission intensity of ZnL_2 in THF/ H_2O mixture increases by a factor of 178 with an increase in the water fraction from 60% to 75%, apparently due to the formation of J-aggregates; the quantum yield reaches 0.33 (in pure THF, $\phi = 0.029$). Furthermore, HL may efficiently detect intracellular Zn (II) ions due to the ESIPT process related to the AIE property of ZnL_2 in the mixed solvent [126].

AIE probes have been developed for the detection of CN^- ions [127]. AIE systems have also shown promise for the detection of other ecologically-important compounds such as carbon dioxide [128], primary amines [129], and hydrogen sulfide [130].

The quenching of the fluorescence of AIE luminogens by various electron receptors has opened additional possibilities for monitoring 2,4,6-trinitrotoluene [131] and even bacteria and toxins, which was stressed in a Faraday Discussions

article related to their practical application [132].

5.4. Biological and Biomedical Applications

Establishing the origin of the AIE effect has motivated the development of AIE structures for biomedical applications such as AIE probes, AIE dots, and AIE photosensitizers. These structures obtained most attention in the photodynamic therapy (PDT) which currently being used as an alternative treatment for the control of malignant diseases [133].

6. PHOTODYNAMIC THERAPY

As known, photodynamic effect is dating from 1900 and associated with O. Raab obtained experimental results in the laboratory of H. Von Tappeiner at the University of Munich. The essence of this phenomenon is that stained by acridine or other fluorescent dyes, such as quinine, methyl phosphine and eosin, *Paramecia* cells (*cilius infusoria*) in the presence of oxygen and visible light was ceased movement and died [134]. The first clinical application of PDT was described by von Tappeiner and Jesionek in 1903, who applied eosin topically to basal cell carcinomas prior to illumination [135]. Von Tappeiner and Jodlbauer later defined PDT as the dynamic interaction among light, a photosensitizing agent, and oxygen resulting in tissue destruction [136]. It took another 70 years, however, before the possibilities of PDT for the treatment of cancer really became recognized.

In 1975, T. Dougherty et al reported the hematoporphyrin derivative (HpD, Photofrin I) in combination with red light (more than 632 nm) could completely eradicate mouse mammary tumor growth and Walker-256 carcinoma in rats [137]. Clinical trials were subsequently carried out initiated with HpD to treat patients with bladder cancer and skin tumors. If in the first studies a tube light source with a filter system was used, then in 1980 laser radiation with a wavelength of 630 nm was successfully applied. A few years later, T. Dougherty with colleagues isolated an active fraction of hematoporphyrin "Photofrin II" differed from "Photofrin I" not only by an increased selectivity of accumulation in tumors but also a more pronounced antitumor effect [138]. These drugs, as their analogues, are the first-generation PS

and, along with high therapeutic activity, have a number of significant drawbacks, and above all, generalized phototoxicity.

In 1990, J. Kennedy et al proposed a fundamentally different approach to PDT, based on the use of endogenous mechanisms of inducing photosensitivity [139]. The idea was based on creation of such conditions in the human organism which would produce a synthesis of an excessive amount of endogenous porphyrins in tumor tissues capable of actively generating singlet oxygen. For this purpose, *d*-aminolevulinic acid, the natural precursor of protoporphyrin IX, and sufficiently active PS with absorption maximum at 630 nm was used. Thus the drugs for fluorescent diagnostics and PDT of keratosis, bladder cancer and brain tumors have been developed.

Today, PDT is an established method of treatment localized cancers. The representative advantage of PDT is ability to destroy cancers without destroying normal tissue structures surrounding the tumor. In addition the treatment can be repeated without cumulative toxicity. PDT advantageously differs from traditional methods of treatment by low invasiveness, high selectivity of tumor destruction, combination in one method of diagnosis and therapy, absence of severe systemic and local complications. Antitumor effects of this type of treatment are due to a combination of direct cell photodamage, destruction of the vasculature of the tumor and an initiate of immune response. The fundamental importance for ensuring the effectiveness of PDT has correctly chosen PS. Nevertheless, despite numerous studies, the encouraging results obtained in anti-cancer PDT using PS, most of PS have some obvious drawbacks, such as lack of specificity and aggregation in aqueous media that limit their use in clinical anticancer PDT. Consequently, the search for an ideal PS is an actual purpose for the further development of PDT.

6.1. Mechanism of Photodynamic therapy

Photodynamic therapy of tumors is based on photophysical and photochemical processes involving PS molecules and described in many articles [53, 55, 140]. An important role in the search of fluorescent molecules as PS is to the classification or

systematics of molecules. According to the systematics the spectral-luminescent properties of molecules are determined by the relative position and proximity of the energy levels of the lowest electron-excited states of different orbital and spin nature which dependent from different structural factors and intermolecular interaction [141-143]. On the basis of this systematics, five spectral-luminescent groups of molecules (SLG) are distinguished (Fig. 15) [144].

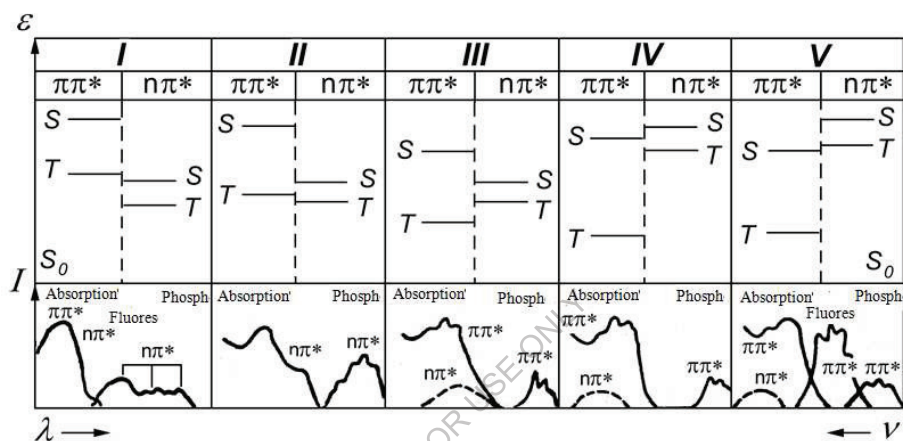


Fig. 15. The basis spectral-luminescent groups of organic molecules and type of absorption and emission spectra [144].

Most of the molecules used to create the PS belong to the V SLG. They have the following location of energy levels: S_0 , $T_{1\pi\pi^*}$, $S_{1\pi\pi^*}$, $T_{2n\pi^*}$, $S_{2n\pi^*}$ and characterized by a significant fluorescence quantum yield, high resistance to photochemical action, which is of great importance for their effectiveness in PDT. At present, the main factors influencing on the relative position of energy levels and, consequently, the fluorescence intensity, emission wavelengths and other fluorescence parameters are established for many heteroaromatic molecules [145, 146].

Based on the knowledge of the electronic structure of the PS molecule, one can proceed to consider the mechanisms of their action. The photophysical processes occur at absorbed and emitted of light by PS molecules can be represented by Scheme (Fig.16).

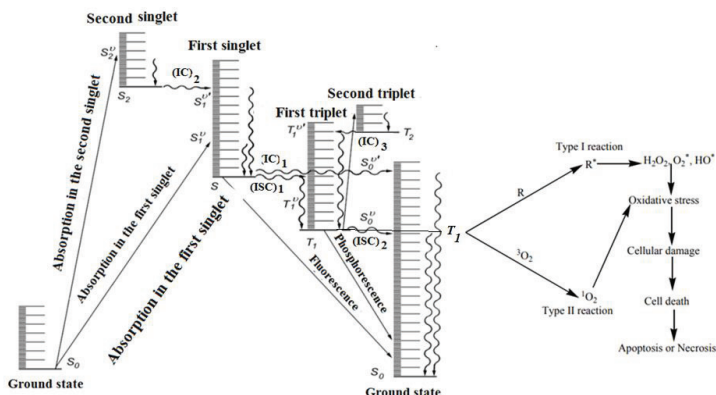


Fig. 16. Modified Jablonski diagram. Photophysical processes involved in PDT: absorption, fluorescence, internal conversion (IC), intersystem crossing (ISC), phosphorescence, formation of free radicals from T_1 PS, and formation of singlet oxygen (1O_2) from triplet oxygen (3O_2) [147].

To obtain a therapeutic photodynamic effect molecules of PS must undergo to its excited triplet state as a result of intersystem crossing ($S_1^* \rightarrow T_1^*$). In addition, the PS can react with different surrounding molecules, generating radicals - type I photoreaction, as well as catalyze the conversion of triplet oxygen (3O_2) into the active excited singlet state by the triplet-triplet energy transfer mechanism (1O_2) - type II photoreaction [148]. The active form of the PS* directly interact with a substrate molecules of the RH cell to form two radicals. The first radical is the hydrogenated form of the sensitizer oxidized by atmospheric oxygen to the original structure of the PS. Another radical - the radical of the substrate - can oxidize other substrates or, adding oxygen, form peroxide radical. Type II oxidative reactions are carried out by singlet oxygen, which is the most destructive species generated in the PDT process [149, 150]. Exactly singlet oxygen generated by the photochemical reaction can directly kill tumor cells and damages the vasculature of the tumor. Cell targets susceptible to reaction with singlet oxygen include unsaturated lipids, cholesterol, α -amino acids (tryptophan) and nucleic acids (guanine) [151].

Currently, some new ideas on the mechanism of photosensitized generation of excited oxygen in the singlet state will facilitate to targeted selection of sensitizers for

photodynamic cancer therapy, are proposed [152, 153]. These mechanisms of activation of singlet oxygen involve energy transfer, which depends on exchange interactions, SOC, charge transfer, intra- and intermolecular vibrations [154, 155].

Thus, under the influence of the energy of light radiation in the cells of microbes or tissues which captured the sensitizer, a photochemical reaction occurs with the generate of singlet oxygen and free radicals - highly active biological oxidants, which are cytotoxic for most biological species and lead to the death and destruction of tumor cells, microorganisms and so on.

The effectiveness of PDT in the treatment of cancer depends on the type of PS, its concentration, intracellular localization, the excitation wavelength of PS and the availability of oxygen. Singlet oxygen generated by the photochemical reaction considerably more efficiently oxidizes the internal elements of cells, which leads to the destruction of internal membranes and can directly kill tumor cells by the induction of apoptosis and necrosis [156]. It also damages the vasculature of the tumor and surrounding healthy vessels, resulting in indirect tumor kill via the induction of hypoxia and starvation. In addition, PDT is able to initiate an immune response against the remaining tumor cells. These mechanisms and treatment regimen can make a certain contribution in the outcome of PDT [157].

6.2. Photosensitizers for Photodynamic therapy

Photosensitizers are molecules absorb light and induce chemical reactions don't occur at their absence [158, 159]. By selecting of PS with corresponding wavelength, it is possible to regulate the penetrating ability of light into biological tissues. After the tumor irradiating the photophysical and photochemical reactions develop in tumor sites containing PS, lead to the death of cancer cells finally. One can conclude about the size and localization of the tumor by the fluorescence intensity of PS. Thus, the success of PDT depends on the correctly selected PS. Now, the main criteria for PS used in PDT have been established:

- absorption spectrum of PS must be in the range of 650 to 850 nm called the “phototherapeutic window” where light penetration into tissue is maximized.

- high photochemical activity of PS characterized by the maximum yield of toxic metabolites of oxygen;
- high affinity and selectivity of accumulation in pathological target-cells with minimal delay in surrounding healthy tissues;
- absence of phototoxicity of degradation products.

The main characteristics of various generations PS are presented in the study [160, 161].

As the first-generation photosensitizers for PDT was investigated a lot of the porphyrin derivatives (hematoporphyrin and its derivative (HpD) [162, 163]. In 1993 the purified fraction of the active material in HpD, porfimer sodium ($\lambda_{\text{abs}}=630$ nm), became the first PS to be approved for PDT. However, porphyrin's PS have some disadvantage, such as light absorption at relatively short wavelengths, low extinction coefficients and prolonged induction of skin photosensitization (1-2 months).

The second generation photosensitizers, includes porphyrins (m-THPP and TPPS4) and related compounds: porphycenes, chlorins, phthalocyanines (Pc4, $\lambda_{\text{abs}}=670-700$ nm); AlPcS4 ($\lambda_{\text{abs}}=676$ nm); AlS2Pc ($\lambda_{\text{ex}}=650-670$ nm), ALA so on [157]. PS second generation are activated by light of more long wavelengths (650-800 nm) penetrated deeper and more selectively accumulates in the tumor tissue. However, the most PS second generation exhibits high hydrophobicity limiting their clinical effectiveness and lead to decreasing of the photodynamic activity or pharmacokinetic problems. The reason for the decrease in activity is the aggregation of molecules leads to poor distribution in the tissue, preventing intravenous use.

Currently, the numerous PS absorbing in a longer wavelength visible and NIR spectral regions (metal complexes of porphyrins, phthalocyanines, etc.), and thereby contribute to the effective destruction of deep-lying tumors were created: tin ethyl etiopurpurin, mono-L-aspartyl chlorin e6, benzoporphyrin derivative, and lutetium texaphyrin. They have absorption bands at relatively longer wavelengths 660, 664, 690 and 732 nm, respectively.

A promising group of PS is 2, 3-naphthalocyanines. Their spectra show a strong bathochromic shift of the long-wavelengths band into the NIR region - up to

800 nm and further. Therefore, they used in therapy in combination with available diode lasers emitting in the NIR spectral region. The difficulty is in the propensity of water-soluble naphthalocyanines to aggregate in solutions greatly decreasing the quantum yield of $^1\text{O}_2$ generation [164]. To eliminate the possibility of aggregation of hydrophobic PSs in aqueous media, water-dispersible nanocarriers have been proposed.

A third generation PS is modification of the second generation PSs with biologic conjugates such as carriers, antibodies or liposomes for improve their physical, chemical and therapeutic properties. These compounds are often actively targeted towards the tumor resulting in higher selectivity. Major biological targets are membranes that undergo rupture and the cells are destroyed through the membranes around the mitochondria and the lysosomes. These organelles induce subsequent cellular destruction by necrosis or apoptosis [160]. An efficient PS of third generation is system composed of the hydrophobic photosensitizer AIPc associated with water dispersible PVM/MA NPs. This system showed improved photophysical and photochemical properties in aqueous media in comparison to the free PS and proved effective against cancerous cells of the murine mammary carcinoma cell lineage 4T1, human mammary adenocarcinoma cells MCF-7 and the mammary epithelial cell line MCF-10A [150].

6.3. Nanoparticles of Photosensitizers creation for Photodynamic therapy

An important step in PDT is pre-determined delivery of PS to tumor target-cells that allows increasing the selectivity of photosensitizer accumulation in the tumor. At present, the possibility of using NPs based on organic and inorganic materials as targeted delivery systems of PS and for visualization of the tumor and therapy is being actively investigated [161].

Nanoparticles containing PS have several advantages over the initial photosensitizing drugs, since they allow increasing the concentration of PS in the target tissue, as well as enhancing their photodynamic activity, despite that the ability of the sensitizer to generate reactive oxygen species decreases [165].

In addition, NPs can be additionally loaded with various compounds, in turn, enhancing the effect of treatment. It has been established that the use of a heterogeneous system of delivery of PS to a tumor as NPs encounters an obstacle on the part of the reticuloendothelial system quickly removes such particles from the bloodstream [166]. However, the coating of NPs with polymers (first of all, PEG) allows solving this problem.

6.4. Nanoparticles based on inorganic and organic materials.

Inorganic nanoparticles are being actively developed to encapsulate PS. A wide range of NIR responsive nanomaterials such as gold nanoparticles, carbon nanotubes, grapheneoxide and upconversion nanocrystals are used as a basis for theranostic applications in PDT. These nanomaterials are able to absorb light in the region outside of tissue autofluorescence, improving imaging quality. Moreover, due to their large surface area, they act as a scaffold on which PSs, targeting moieties, other diagnostic agents and other therapeutics can be assembled [167].

The systems based on metal and metal oxide NPs, for example, noble metal NPs (silver and gold) have been created. Immobilization of PS on nanocarriers allows increase their bioavailability, to reduce influence on the organism as a whole, by purposefully influencing the tumor area. It is possible to achieve an increase in the quantum yield of reactive-oxygen-species (ROS) generation in systems containing of gold NPs. It is attractive to use as a carriers PS of a double hybrid system containing both polymers and gold NPs simultaneously [168]. According to this principle a composite PS consisting of gold NPs in a copolymer dextran-polyacrylamide matrix and chlorin e6 was created. Nanocomposite PS in in vitro experiments with malignant cells of the MT-4 line showed photodynamic antitumor activity of 2-fold higher than of free chlorine e6. High antitumor photodynamic activity of the nanocomposite was confirmed in experiments in vivo in mice with transfused Lewis lung carcinoma.

In [169] indocyanine green (ICG)-loaded hollow mesoporous silica NPs (ICG/HMS NPs) are described. When the ICG NPs are loaded into the HMS NPs, they are forced to aggregate and as a result, fluorescence and singlet oxygen

generation of photosensitizer-loaded HMSNP becomes self-quenched (i.e. turned off) because of the fluorescence resonance energy transfer between ICG molecules. After the NPs enter the cancer cells via endocytosis, they become strongly fluorescent and phototoxic. In addition, intracellular absorption of the ICG nanosystem in HMSNP becomes 2.75 times higher than of free ICG, resulting in an enhanced phototherapy of cancer.

When creating nanoparticles based on organic materials PS can be encapsulated in such delivery agents such as liposomes, micelles, and polymers. The liposomes of various structures are used as carriers for PS [170]. The PS can be encapsulated either in the aqueous phase of liposomes or in their lipid bilayers, depending on its hydrophilicity [171]. So, for example, to improve the selectivity of photoditazine (PS based on chlorine e6 derivative) accumulation in the tumor tissue, a liposome composite of photoditazine was created [172].

A variation of the targeted transport system is the conjugation of PS with oligonucleotides, proteins and other biostructures or their fragments. An example of such a transport system is presented in study [173]. Nanoparticles of a folate-modified copolymer of PLGA were used to deliver pheophorbide (Pba) to the tumor. The obtained NPs of folate-PLGA-Pba have been increased the effect of absorption and death of human gastric cancer cells MKN28. The pronounced fluorescence of Pba showed high accumulation of FA-PLGA-Pba NPs in tumor site in the MKN28 tumor muscle model.

A similar encapsulation of PSs into amphiphilic polymer of hyaluronic acid (HA) NPs is presented by Yoon et al in [174]. The hyaluronic acid NPs were used for delivery of the hydrophobic PS, chlorin e6 (Ce6).

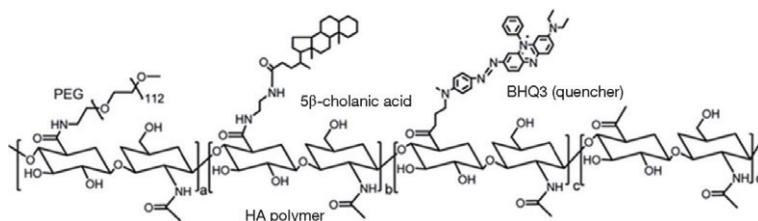


Fig. 17. Chlorin e6-loaded hyaluronic acid nanoparticles.

The chemical conjugation of aminated 5 β -cholanic acid, PEG and BHQ3 to the HA backbone resulted in self-assembled HA NPs (Fig. 17). The strategy for targeting the tumor site with the HA NPs is based on the binding of HA to CD44 receptors. Ce6-loaded-HA NPs rapidly released Ce6 in the tumor tissue due to the degradation of the HA backbone in presence of the hyaluronidase abundant in the cytosol of tumor cells. After 30 min of incubation with Ce6-HA NPs, a fast cellular uptake and intracellular fluorescence generation of Ce6-HA NPs in HT29 cells, and the fluorescence intensity enhancing was observed. HT29 cells treated with Ce6-HA NPs were damaged after 2 min of irradiation with an NIR laser, and their viability was lower than 10%.

6.5. Nanoparticles of photosensitizers with an aggregation-induced emission effect

In contrast to traditional photosensitizers characterized by fluorescence quenching and inefficient generation of active oxygen forms in the aggregate state, AIE photosensitizers as nanoaggregates demonstrate stronger fluorescence, which permits the accumulation of higher active oxygen concentrations [175-177].

An archetypical AIEgen is tetraphenylethene (TPE), with four phenyl rings freely connected to a central olefin structure. In solution state, the rotation of these rings provides a non-radiative way of dissipating exciton energy and as a result, TPE has almost no fluorescence in dilute solution. However, when TPE is aggregated by, for example, the introduction of a poor solvent such as water, rotation is physically restrained (referred to as the restriction of intramolecular motion) and, moreover, the twisted structure of this molecule hinders π - π stacking interaction. This process leads to the emergence of fluorescence AIE. This property produces interesting opportunities for using TPE in PDT. AIE effect can be used to create NPs or dots with bright fluorescence, due to the aggregation of fluorophores inside the NPs. Also, it can be used to produce of some kind of responses to the environment and enables the imaging and subsequent localization of the PDT (image-guided therapy).

Using a pronounced emission of AIE-luminogenes in an aggregated state, AIE-dots were created. AIE-dots are very small organic nanoparticles with different

functionalities demonstrated high brightness, strong photobleaching resistance and excellent biocompatibility. AIE-dots successfully used in targeted cellular and subcellular imaging, as well as in tracking cancer cells in vitro and in vivo [178-182]. The recent development of AIE dots with emission in the near-IR region has opened new and expanded possibilities for visualization, operational surgery, and therapy [183].

TPE-TPA-DCM possesses both TICT and AIE features was synthesized and fabricated its BSA NPs show efficient FR/NIR fluorescence with low cytotoxicity [184]. Upon addition of the TPE-TPA-DCM solution in THF to the aqueous solution of BSA, the TPE-TPA-DCM molecules aggregate and the fluorogen-loaded BSA NPs form instantly. The emission maximum of the fluorogen-loaded BSA NPs is located at 668 nm. The ϕ_f values of the fluorogen-loaded BSA NPs reached of 12% at a fluorogen loading of 3.07 wt %. It was founded that fluorogen-loaded BSA NPs can be successfully used for in vitro and in vivo FR/NIR bioimaging for MCF-7 breast-cancer cells and a murine hepatoma-22 (H₂₂)-tumor-bearing mouse model, respectively.

The ability to image single-cell migration in real time is important to many areas of research, such as the detection of cancer metastases, cell therapy and the immunology of lymphocytes. Understanding genesis, development, invasion and metastasis of cancerous cells require continual tracing of the biological processes by cytocompatible fluorescent probes over a long period of time. The FR/NIR fluorogen TPAFN as adduct of triphenylamine (TPA) and fumaronitrile (FN) with AIE-effect was designed and then TPE attached to TPAFN to produce TPETPAFN, which is a sample novel class of promising long-term cell tracing probes [179, 181]. The pure THF solution of TPAFN shows weak red fluorescence with an emission maximum at 652 nm. With gradual addition of water into THF (water fractions, $f_w < 70$ vol. %) the emission of TPAFN is weakened and shifted from 652 to 665 nm. TPAFN molecules cluster into nanoaggregates due to the poor solubility and the emission is dramatically enhanced showing an obvious AIE effect when $f_w > 70$ vol. %. In addition, the emission maximum shift back to 655 nm similar to pure THF. The emission intensity

at $f_w = 90$ vol. % is 12-fold higher than in pure THF solution. The ϕ_f of TPAFN and TPETPAFN in THF are as low as 2.32 and 0.59 %, while their ϕ_f in solid state reached 42.5 and 52.5 %, respectively. Further, the TPETPAFN-loaded lipid-PEG-encapsulated AIE dots with surface cell penetrating peptide for noninvasive in vitro and in vivo cancer cell tracing were created. Bioconjugation of the AIE dots with cell penetrating peptide derived from HIV-1 transactivator of transcription (Tat) protein, yielded Tat-AIE dots with high cellular internalization efficiency. It was founded the Tat-AIE dots could trace MCF-7 cells for 10–12 generations in vitro and C6 cells for 21 days in vivo [179].

So far, AIE NPs (polymer NPs and silica NPs) with blue to NIR emission have been successfully developed and applied to in vitro and in vivo applications [182]. However, the currently available NIR AIE NPs have emission spectra below 700 nm with absorption maxima below 500 nm. To obtain NIR-fluorescent AIE NPs with red/NIR absorption, the employed molecules should have a narrow band gap and AIE characteristics and their emission maximum of AIE NPs in the range of 780–820 nm.

To realize this goal, two series of donor–acceptor–donor (D–A–D) structured compounds: α -DTPEBBTD- C_x and β -DTPEBBTD- C_x were designed and synthesized (Fig. 18) [183]. The monoalkoxy-substituted TPE as an electron donor is formed D–A–D structures with BBTD as an electron acceptor resulting to yield NIR emissive AIE molecules with desirable absorption and emission maxima for in vivo imaging applications. It should be noted that β -DTPEBBTD- C_x consists of isomers due to the geometrical difference in the positions of monoalkoxyphenyl groups, but α -DTPEBBTD- C_x does not.

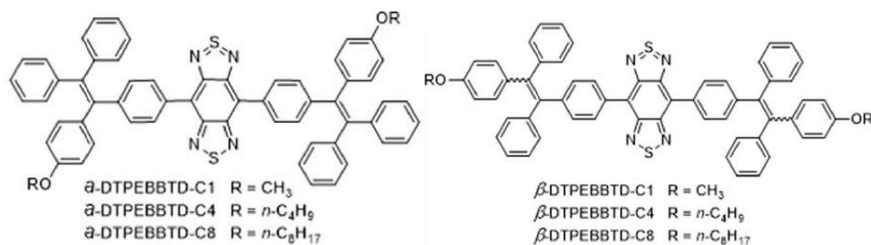


Fig. 18. Structures of D–A–D compounds: α -DTPEBBTD- C_x and β -DTPEBBTD- C_x (x - the number of carbon atoms of the alkoxy chain on the TPE blocks, and x is 1, 4 or 8).

All of the compounds show higher fluorescence intensities in aggregates than in pure THF, indicative of AIE characteristics. Interestingly, the extent of fluorescence enhancement is generally increased with the alkoxy chain length. In addition, when the molecules aggregate in less polar environment than water the gradual blue shifts are observed for the emission maxima when f_w changes from 50 vol.% to 90 vol.% (from 836 nm to 798 nm for α -DTPEBBTD- C_x and to 816 nm for β -DTPEBBTD- C_x). These results supported the molecules not only show AIE characteristics but also have emission maxima in the 780–820 nm range. The ϕ_f of the AIE NPs is gradually increased when longer substituents are used (from 3.8% to 4.8% for α -DTPEBBTD- C_x and from 2.2% to 3.8% for β -DTPEBBTD- C_x). The obtained NIR fluorescent α -DTPEBBTD- C_4 NPs have been successfully applied to NIR fluorescence image-guided cancer surgery. They have demonstrated great potential in high accuracy tumor detection with a high tumor-to-normal tissue ratio of 7.2, which enabled the surgeons to perform image-guided surgery to remove tiny tumors [183].

The molecule with two triphenylamine, an AIEgen, and two TPE moieties and a red-emitting TTD part in the center was used to create AIE-dots. Encapsulation of TTD using DSPE-PEG-Mal as the encapsulation matrix, followed by surface functionalization with the target moiety of the cRGD tripeptide were prepared the targeted TTD NPs (T-TTD NPs) with a mean size of ~ 30 nm (Fig. 19) [185]. The T-TTD NPs show bright red fluorescence with an emission maximum at 660 nm. To test the targeting effect of T-TTD NPs, MDA-MB-231 cancer cells with overexpressed $\alpha v \beta 3$ integrin on the cellular membrane were chosen as integrin-positive cancer cells which then were incubated and the red fluorescent signals in MDA-MB-231 cells were observed at different incubation time points.

The ROS production by T-TTD NPs after cancer cell uptake was evaluated with using the fluorescent dye DCF-DA. The strong green fluorescence of DCF was observed inside the cells, demonstrating efficient ROS generation from the T-TTD NPs. Cell viability studies showed the T-TTP NPs could selectively and efficiently kill cancer cells with overexpressed $\alpha v \beta 3$ integrin.

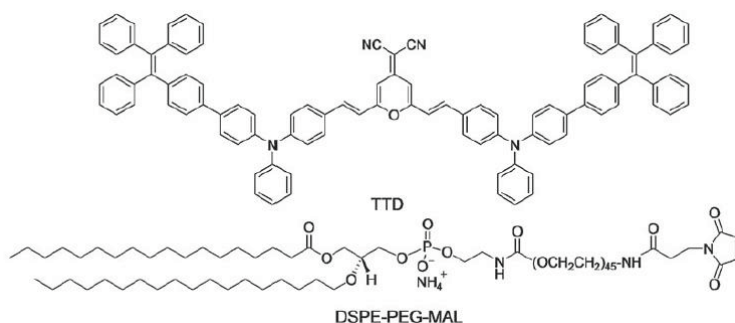


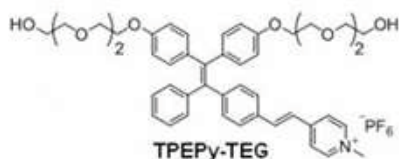
Fig. 19. Schematic illustration of T-TTD NPs formation

Li et al. attached cRGD to the end of the amphiphilic PEG, targeting integrin $\alpha v \beta 3$ overexpressing cholangiocarcinoma cells (CC) [186]. The T-TTD dots were prepared by a modified nanoprecipitation method using DSPE-mPEG and DSPE-PEG2000-cRGD to form NPs with TTD molecules encapsulated as the hydrophobic core and cRGD exposed to the aqueous media. The emission spectra of T-TTD dots have maximum at 660 nm. The ROS quantum yield of T-TTD dots was determined to be 0.51, which is comparable to clinically used PSs such as Photofrin ($\phi = 0.28$) or Laserphyrin ($\phi=0.48$). Thereby, the obtained AIE-dots showed high specificity for CC, and also had an excellent antitumor effect both in vitro and in vivo.

The fluorescent probe systems DPBA-TPE with the AIE characteristics emits strong red fluorescence and can efficiently generate ROS in the state of aggregates are presented in [187]. As known, the first generation of AIE probes for biological detection was based on changes in the fluorescence of water-soluble AIE luminogens due association-dissociation processes with the analytes used for studying the activity of enzymes and screening inhibitors. The invention of special AIE biosensors such as peptide AEI conjugates has permitted continuous monitoring of cell apoptosis in real time and the development of biomarkers for cancer cells [188, 189]. This principle also led to the rapid development of various probes for the detection and tracing of various biomolecules and small molecules in vitro and in vivo [190-191]. Using the unique structure of AIE photosensitizers, the AIE photoprobe can be immediately transformed into a therapeutic probe to perform simultaneous probing, visualization,

and therapy [192, 193]. Light probes with activated photoactivity have been developed for the controlled ablation of cancer cells [194, 195]. Similar probes have been found effective for the detection, visualization, and ablation of bacteria [196, 197]. AIE-based supramolecular nanostructures exhibit excellent photodynamic activity in aggregate, offering great potential for diagnosis of pathogen, but also image-guided PDI therapy for pathogenic infection [198].

The small-molecular-weight AIEgen tracer, TPEPy-TEG, for tracking of



individual embryonic cell proliferation and differentiation with bright signals was designed [199]. This AIEgen tracer has several advantages compared with the commonly used tracers, such as HRP and fluorogen–dextran conjugate such as large

Stokes shift of 330 nm in water, high photostability, good biocompatibility, and the two hydrophilic TEG arms endow TPEPy-TEG with poor cell permeability.

So, DPBA–TPE in THF showed an absorption maximum at 480 nm and weak orange–red fluorescence with the emission maximum at 619 nm. The AIE properties of DPBA–TPE were analyzed by measuring its photoluminescence spectrum changes in water/THF mixtures with different values of f_w . It was established the enhancing of DPBA–TPE emission with increasing of $f_w \approx 50\%$. These data indicate the DPBA–TPE possesses AIE characteristics.

The ability of the DPBA–TPE system to generate ROS in aggregated state was studied also. The mixed aqueous solution of DPBA–TPE ($10 \cdot 10^{-6}$ M) showed quickly increased fluorescence at 530 nm upon exposure by white light irradiation (250 mWcm^{-2}) within minutes, indicating the DPBA–TPE aggregates are able to efficiently generate singlet oxygen species. Based on DPBA–TPE and PEG derivatives with a folic acid (FA) fragment, nano-sized dots with bright red fluorescence and high ROS generation for cellular and mitochondrial dual-targeting were fabricated [187]. To delivery of AIE dots to mitochondria, cationic TPP able to accumulate in mitochondria in response to high mitochondrial membrane potential

was then reacted with AIE dot suspension to yield FA–AIE–TPP dots. The folate acid promotes the cellular uptake to folate receptor (FR)-positive cancer cells, and TPP drives AIE dots to accumulate in mitochondria. Cell viability studies revealed the dual-functionalized FA–AIE–TPP dots showed more efficient anticancer PDT effects than single-ligand-functionalized AIE–TPP or AIE–FA dots. Thus, FA-AIE-TPP dots for specific targeting of FR-positive mitochondria of MCF-7 human breast carcinoma were yielded.

To achieve the mitochondrial targeting the various cationic lipophilic fluorescent dyes attracted to mitochondria due to large values of the membrane potential ($\Delta\Psi_m$) have been develop now. The value $\Delta\Psi_m$ is a critical parameter reflecting the mitochondrial functional status and cell viability [200]. However, the photostability of these dyes is extremely low due to the concentration quenching emission effect [201]. To solve this problem the potential of AIE-luminogens is widely used at present. Due to the AIE effect, the photostability of these probes has improved significantly. However, most of these probes emit in a short wavelength region and are unresponsive to the changes of $\Delta\Psi_m$. On the other hand, probes emitting in a longer wavelength region offer various advantages such as minimum photodamage to biological samples, deep tissue penetration. An example of such luminogen is a mitochondrial specific AIE-luminogen, TPE-Ph-In, obtained by incorporating indole salt into the TPE [202]. TPE-Ph-In emits weakly in DMSO. The emission of TPE-Ph-In is enhanced about 70 times upon the formation of aggregates when the $f_w \approx 99\%$ in the solvent mixture DMSO/H₂O. At that condition the stronger red fluorescence at 670 nm was observed. Thus, TPE-Ph-In is an AIE active. More importantly, the fluorescence signals of TPE-Ph-In can directly represent $\Delta\Psi_m$ based on the positive correlation between the fluorescence intensity and the local dye concentration in mitochondria. The possibility of applying TPE-Ph-In for determine of the change $\Delta\Psi_m$ in living cells was confirmed with membrane-potential stimulants, oligomycin and carbonyl cyanide 3-chlorophenylhydrazone which treated the cells prior to the staining process and recorded a change in fluorescence.

The using of TPE conjugated with dicyanovinyl promoted the production of high two-photon absorption cross section, thereby a promising two-photon imaging technology was established [203]. The conjugation of TPE to benzothiazole derivatives facilitate to self-assembled into NPs demonstrate efficacy on PC3 human prostate cancer cells, both in vitro and in vivo [198].

Mitochondria-targeting NPs using AIE cross-linked copolymer (PAIE-TPP), decorating with TPP as the mitochondria-target group and possessing the segments of AIE monomer AEMA and HPMA were fabricated (Fig. 20) [204]. The average diameter of PAIE-TPP NPs is 260 nm. TPP can direct NPs specifically to mitochondria, and then generate ROS at specific sites and lead to mitochondrial collapse and apoptosis of the cells. Namely, pH-sensitive linker allowed the PEG layer to be shed once the NPs were in an acidic environment of tumor cells, after which the TPP moiety on the NPs allowed mitochondrial targeting. It is confirmed the UCNPs, together with the AIEgen generate ROS efficiently under NIR irradiation, which allowed effective PDT against A549 human lung cancer cells. The obtained NPs with a cross-linked copolymer not only emit a enhancement far-red/near-infrared (FR/NIR) fluorescence, but also generate high reactive oxygen activity (77,9 %) [205].

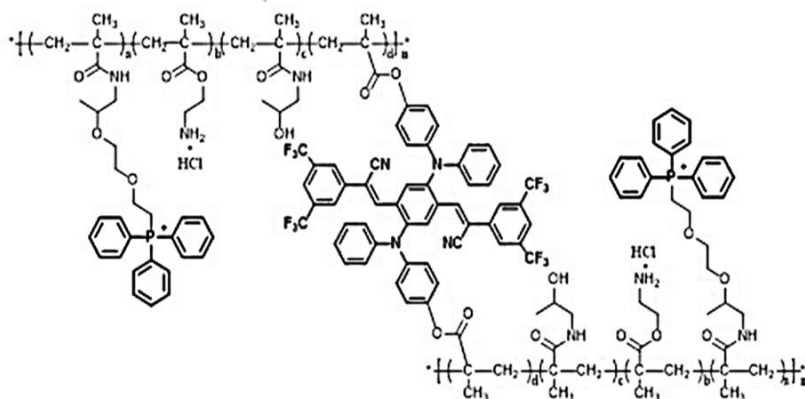


Fig. 20. Schematic illustration of the PAIE-TPP NPs as mitochondria-targeted agents

The small energy gap (ΔE_{ST}) between the lowest singlet-excited state (S_1) and the lowest triplet-excited state (T_1) is favorable for ISC to process efficiency ROS generation. The ΔE_{ST} of AIEM is around 0.277 eV, such a small ΔE_{ST} is expected to promote the ISC process efficiently, benefiting ROS generation [205].

TPE derivative conjugated to the peptide chain and cRGD was used to create a cathepsin B sensitive probe. Cathepsin B is a lysosomal protease overexpressed in many types of tumors [206]. An activatable probe can be created by incorporating a target ligand and a substrate that can be cleaved by cathepsin B. Cathepsin B sensitive probe is possible to achieve highly specific cancer cell killing as a result of the dual selection processes [207]. The probe is composed of four parts: 1) an orange fluorescent AIE fluorogen as animaging reagent and photosensitizer, 2) a GFLG peptide substrate that is responsive to cathepsin B, 3) a hydrophilic linker with three Asp (D) units to increase the hydrophilicity of the probe, and 4) a cRGD-targeting moiety (Fig. 21).

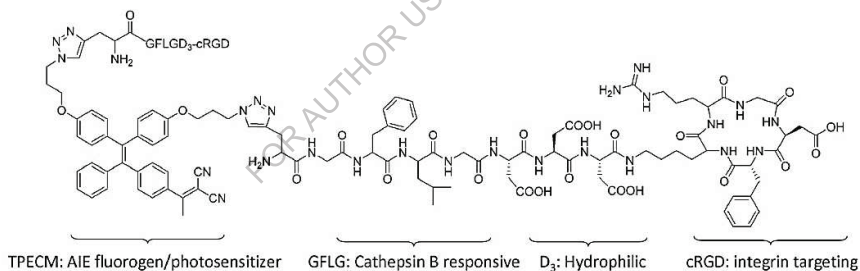


Fig. 21. Schematic illustration of bioprobe TPECM-2GFLGD3-cRGD.

As AIE fluorogen was used TPE. The incorporation of dicyanovinyl groups into TPE yielded to shift of emission from orange to red region. To test whether the dicyanovinyl-modified TPE derivative retained the AIE properties, the fluorescence intensity of TPECM-2N₃ in DMSO/H₂O mixtures with different f_w was studied. TPECM-2N₃ was found to be almost non fluorescent in DMSO. However, as f_w value increased to 99%, the fluorescence intensity increased at 105 times on comparison with DMSO. These results indicate the dicyanovinyl-modified TPE retains AIE properties. The probe itself is almost nonfluorescent in aqueous media. After cancer-

cellular uptake, cleavage of the GFLG substrate by cathepsin B should lead to enhanced fluorescence signal output concomitant with activated photoactivity. For presented probe, a steady fluorescence increase of the probe solution during incubation for 60 min with cathepsin B in DMSO/buffer (1:199, v/v) was observed. The increasing of fluorescence at 35-fold higher than the intrinsic emission of the probe was observed. Aggregate formation clearly explains the probe fluorescence turn-on in the presence of cathepsin B. The key role in probe properties has its low cytotoxicity. The evaluation of the cytotoxicity of the probe to MDA-MB-231, MCF-7, and 293T cells upon incubation for 24 h in the dark shown no significant cytotoxicity for any of tested cells, even when the probe concentration reached 50 μm . However, upon irradiation with light, a dose-dependent cytotoxicity was observed in MDA-MB-231 cells and in MCF-7 and 293T cells only minimal toxicity. At the same time, when MDA-MB-231 cells were pretreated with cRGD decreased cell death was observed in agreement with the apoptosis studies. Furthermore, the probe-stained MDA-MB-231 cells were exposed to irradiation with light for different durations. It was observed a stronger inhibition of cell viability with a longer laser irradiation time [207].

To identify solid tumor cells the biosensor (TPPP, Fig. 22) consisting of a PS PpIX and an AIE molecular TPE using PEGylated PLGVR peptide sequence as a linker was proposed [208]. When TPPP arrive at the tumor tissue, the overexpressed MMP-2 in tumor region hydrolyzed the PLGVR sequence, leading to the detachment of TPE demonstrating the AIE-effect and PEGylated PpIX.

The ratiometric fluorescence ratio between TPE and PpIX could evaluate the MMP-2 expression level. On the other hand, this AIE-effect provided a visible and accurate feedback of the photodynamic time and region. The efficient SCC-7 tumor accumulation of TPPP under light irradiation leads to enhanced therapeutic efficacy with reduced side effects. The intravenously injected with TPPP solution with 20-min light irradiation inhibit the growth of tumor significantly suggesting the good antitumor efficacy of TPPP under light irradiation.

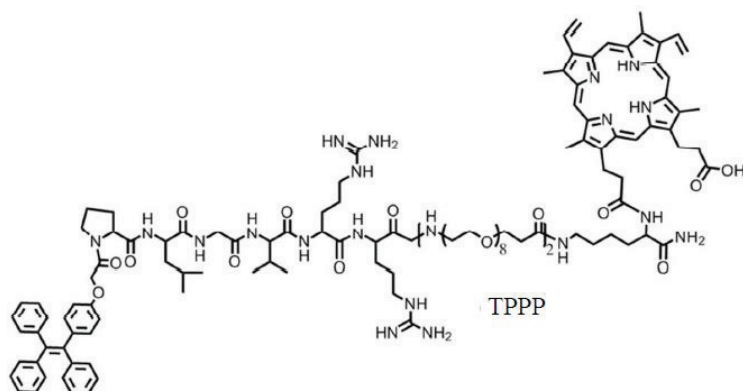


Fig. 22. Schematic illustration of biosensor TPPP

Based on AIEgen TPE-red with an outstanding ability to produce ROS the dual-function AIE NPs for the purposeful and visual-guided PDT in vivo targeting UMUC3 cells (human bladder cancer cell line), HeLa (human cervical cancer cell line), and A549 (human lung carcinoma cell line) were fabricated [209]. To enhance tumor targeting, promote endocytosis and ensure a therapeutic effect, the NPs were modified with a customized peptide, c(RGDfc), a group commonly used to target overexpressed integrin $\alpha v \beta 3$ in most cancerous cells. TPE-red weakly emissive in pure THF while the intensity fluorescence of TPE-red-PEG-RGD NPs at 9.5-fold higher than TPE-red. The main advantage of TPE-red-PEG-RGD NPs consist of the high antitumor efficiency could be achieved at a reasonably low dose, and thereby to cause the fewer of the side effects.

The series of new tetraphenylethylene isoquinolinium TPE-IQ-based AIEgens namely TPE-IQ-O, TPE-IQ-CN, and TPE-IQ-triphenylamine (TPA) (Fig.23) were prepared [210]. They all exhibited AIE characteristics with different emission colors and Zeta potentials when aggregated as nanoparticles. These compounds were faintly emissive in THF solutions with quantum yield $\phi = 1.6\text{--}2.3\%$, which were enhanced in the solid powders with $\phi = 11.4\text{--}16.2\%$. The ability of ROS generation for TPE-IQ-based AIEgens upon white light irradiation was evaluated. It was founded that in the presence of TPE-IQ-based AIEgens, the emission intensity indicator and exhibited

the “turn-on” fluorescent signal activated by ROS gradually enhanced over 20-fold to 45-fold with the increase of irradiation time by white light. It was shown that created AIEgens TPE-IQ-O could specially target mitochondria and while TPE-IQ-CN and TPE-IQ-TPA could target lysosome instead.

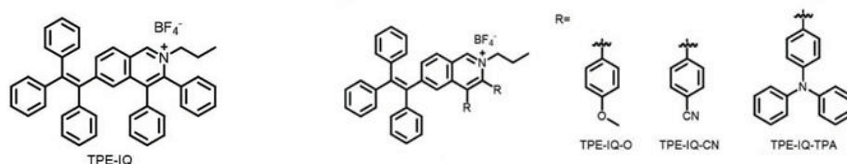


Fig. 23. Molecular structures of TPE-IQ, TPE-IQ-O, TPE-IQ-CN, and TPE-IQ-TPA

The efficient image-guided candidates for cancer treatment are AIE structures based on organometallic and coordination compounds [211, 212]. For example, cyclometalated Ir (III) complexes IrBDP could self-assemble into organic nanoparticles (IrBDP NPs) and show enhanced photodynamic effect promote their use for cell imaging, as well as carrying out PDT under low energy irradiation [213]. The IrBDP complex emits with a maximum at 526 nm, however, as a result of self-association in water the maximum of emission shifted to 554 nm. Phototoxicity of IrBDP NPs against murine colon cancer (CT26) and HeLa cell line was validated. In order to demonstrate the cell death mechanism, the cells apoptosis experiment was conducted. The experiment showed significantly increasing in apoptosis rate of CT26 cells to 85.1 % from 12.36% and HeLa cells to 69.8% from 2.555% under treatment with IrBDP NPs upon irradiation. These results manifest that the IrBDP NPs possess excellent photodynamic effect.

Cancer cells with vasculature configuration and over proliferation of neoplastic cells have an altered mitochondrial redox state, typically characterized by high levels of reactive oxygen species (ROS) and antioxidants, such as glutathione (GSH). GSH can react with ROS, which can reduce the damage of ROS to the cancer cells. Therefore, it has been recognized that disrupting the redox homeostasis can be a potential strategy for cancer treatment. Depletion of antioxidants, such as GSH, will

amplify intracellular oxidative stress, thereby triggering cancer cell death and enabling more effective cancer treatment. In study [214] presented two kinds of GSH responsive pyrrolopyrrolidone (DPP) derivatives that conjugated with 2-(diphenylmethylene) malononitrile (DPPBPh) and 2,3,3-triphenylacrylonitrile (DPPTPh), and their corresponding NPs for combination cancer (Fig. 24.). In the photoluminescence spectra, DPPBPh and DPPTPh in THF show the emission peaks at 649 nm, 710 nm and 651 nm, 711 nm, respectively. The large Stokes shift was also observed for those nanoparticles in water (727 nm, 808 nm for DPPBPh and 728 nm, 808 nm for DPPTPh), which can be ascribed to the aggregation of these compounds.

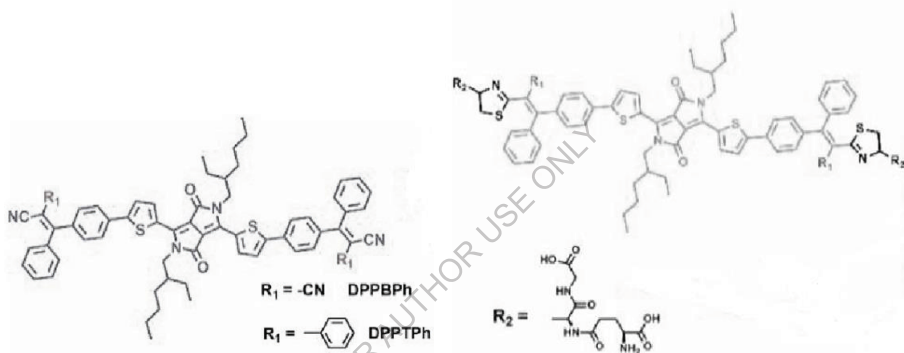


Fig. 24. Schematic illustration of structure of GSH responsive DPP derivatives

These compounds after adding water to THF formed spherical NPs with hydrodynamic size distribution between 34 to 135 nm for DPPBPh and 58 to 192 nm for DPPTPh, respectively. It was founded the fluorescence intensity of DPPBPh and DPPTPh after reaction with GSH was 6 and 8 times higher than that of the original ones, indicating that the two compounds can be used as colorimetric GSH probes to avoid the fluorescence quenching caused by aggregation.

CONCLUSIONS

In summary, we demonstrated that PSs on the base of AIE-luminogens can be effective tools in monitoring of many important biological processes in clinic of PDT. The application of the AIE-luminogens as PSs which show high emission and

efficient ROS production in the aggregated state will provide a straightforward solution to the problem of ACQ. In addition, the application of AIE-fluorophores emitting in the FR/NIR is beneficial to high penetration depth in tissue and low biological autofluorescence interference in bioimaging and PDT applications. The creation of NPs with AIE-effect based on organic or inorganic materials through physical interactions will provide targeted delivery of PS to the tumor, its visualization and subsequent localization of therapy (image-guided therapy).

In general, the development of PS with the AIE effect will expand their use in biomedical research, including for visualization in vitro and in vivo of biological structures (organelles, cells, tissues etc.) and in the studies of cellular processes (apoptosis, metastases, etc.). The obtained results of the researches will be applied in the complex problems of the PDT which can't solved by traditional strategies.

REFERENCES

1. Gaponenko S.V. Optical Properties of Semiconductor Nanocrystals, University Press, Cambridge. Cambridge Studies in Modern Optics (Book 23). 1998; 260 p.
2. Rogach A. (ed.). Semiconductor Nanocrystal Quantum Dots. Synthesis, Assembly, Spectroscopy, and Applications, Springer. New York. 2008; XI: 372 p.
3. Chen M., Sun J. Z., Qin A. J. and Tang B. Z. Heterocycle-based luminogens with aggregation-induced emission characteristics. Chinese Sci. Bull. 2016; **3**: 304-314.
4. Liu G. G., Chen D. D., Kong L. W. et al. Red fluorescent luminogen from pyrrole derivatives with aggregation-enhanced emission for cell membrane imaging. Chem. Commun. 2015; **51**: 8555-8558.
5. Stewart M. E., Anderton C.R., Thompson L.B. et al. Nanostructured plasmonic sensors. Chem. Rev. 2008; **108**(2): 494-521.
6. K. Li and B. Liu, Polymer-encapsulated organic nanoparticles for fluorescence and photoacoustic imaging. Chem. Soc. Rev. 2014; **43**(18): 6570-6597

7. Kim H. Y., Bjorklund T. G., Lim S.-H. and Bardeen C. J. Spectroscopic and Photocatalytic Properties of Organic Tetracene Nanoparticles in Aqueous Solution. *Langmuir*. 2003; **19**: 3941-3946.
8. Wenus J., Ceccarelli S., Lidzey D. G. et al. Optical strong coupling in microcavities containing J-aggregates absorbing in near-infrared spectral range. *Org. Electron*. 2007; **8**(2/3): 120-126.
9. Luo J., Xie Z., Tang B. Z. et al, Aggregation-induced emission of 1-methyl-1,2,3,4,5-pentaphenylsilole. *Chem. Commun*. 2001; **18**: 1740-1741.
10. Chen J., Law Ch.C.W., Tang B.Z. et al. Synthesis, Light Emission, Nanoaggregation, and Restricted Intramolecular Rotation of 1,1-Substituted 2,3,4,5-Tetraphenylsiloles. *Chem. Mater*. 2003; **15**(7): 1535-1546.
11. Chen J., Xie Z., Tang B. Z. et al. Silole-Containing Polyacetylenes. Synthesis, Thermal Stability, Light Emission, Nanodimensional Aggregation, and Restricted Intramolecular Rotation. *Macromolecules*. 2003; **36**(4): 1108-1117.
12. Vonnegut C.L., Tresca B.W., Johnson D.W. et al. Ion and Molecular Recognition Using Aryl-Ethynyl Scaffolding. *Chem. Asian J*. 2015; **10**(3): 522-535.
13. Deans R., Kim J., Machacek M. R. et al. Poly(p-phenyleneethynylene) with a Highly Emissive Aggregated Phase. *J. Am. Chem. Soc*. 2000; **122**(35): 8565-8566.
14. Belton C., O'Brien D. F., Blau W. J. et al. Excited-state quenching of a highly luminescent conjugated polymer. *Appl. Phys*. 2001; **78**(8): 1059-1061.
15. Zhao C.H., Sakuda H., Wakamiya W., and Yamaguchi S. Chem. Highly Emissive Diborylphenylene-Containing Bis(phenylethynyl)benzenes: Structure-Photophysical Property Correlations and Fluoride Ion Sensing. *Eur. J*. 2009; **15**(40): 10603-10612.
16. Fu H.-B. and Yao J.-N. Size Effects on the Optical Properties of Organic Nanoparticles. *J. Am. Chem. Soc*. 2001; **123**(7): 1434-1439.

17. An B.-K., Kwon S.-K., Jung S.-D. et al. Enhanced Emission and Its Switching in Fluorescent Organic Nanoparticles. *J. Am. Chem. Soc.* 2002; **124**(48): 14410-14415.
18. Su X., Zhang H., You K. et al. Barbituric Derivative Nanoaggregates with Aggregation-Induced Emission and Mechanofluorochromism. *Journal of Nanomaterials*. Volume 2019, Article ID 7635756, 10 pages <https://doi.org/10.1155/2019/7635756>
19. Yin G., Ma Y., Xiong Y. et al. Enhanced AIE and different stimuli-responses in red fluorescent (1,3-dimethyl)barbituric acid-functionalized anthracenes. *J. Mater. Chem. C*. 2016; **4**: 751-757.
20. Gao H., Bao P., Dai S. et al. Far-Red/Near-Infrared Emissive (1,3-Dimethyl)barbituric Acid-Based AIEgens for High-Contrast Detection of Metastatic Tumors in the Lung. *Chem. Asian J.* 2018; 10.1002/asia.201801660
21. Ibrayev N. Kh., Yeroshina S. A., Ishchenko A. A., and Mushkalo I. L. Investigation of conformational and electron properties of biscyanine dyes. *Mol. Cryst. Liq. Cryst.* 2005; **427**(1): 139-147.
22. Ibraev N. Kh., Ishchenko A. A., Karamysheva R. Kh., and Mushkalo I. L. Influence of interaction of chromophores, linked by the unconjugated chain, on the luminescence properties of biscyanine dyes. *J. Lumin.* 2000; **90**(3/4): 81-88.
23. Ishchenko A. A. and Shapovalov S. A. Nanostructured plasmonic sensors. *J. Appl. Spectrosc.* 2004; **71**(5): 605-629.
24. Nekrasov A.D., Shapiro B.I., Tolmachev A.I., et al. Effect of organic polyelectrolytes on H^{*}-aggregation of meso-methylsubstituted thiacyanine dyes *High Energy Chemistry*. 2011; **45**(6): 525-531.
25. McRae E.G. and Kasha M. Enhancement of Phosphorescence Ability upon Aggregation of Dye Molecules. *J. Chem. Phys.* 1958; **28**(4): 721-722.
26. Kasai H., Yoshikawa Y., Seko T. et al. Optical properties of perylene microcrystals. *Mol. Cryst. Liq. Cryst.* 1997; **294**(1): 173-176.

27. Kasai H., Kamatani H., Okada S. et al. Size-Dependent Colors and Luminescences of Organic Microcrystals. *Jpn. J. Appl. Phys.* 1996; **35**, Pt 2(2B): L221-L223.
28. Kasai H., Kamatani H., Yoshikawa Y. et al. Crystals Size Dependence of Emission from Perylene. *Chem. Lett.* 1997; **26**(11): 1181-1182.
29. Komai Y., Kasai H., Hirakoso H. et al. Size and Form Control of Titanylphthalocyanine Microcrystals by Supercritical Fluid Crystallization Method. *Mol. Cryst. Liq. Cryst.* 1998; **322**(1): 167-172.
30. Xu Y., Xue P., Xu D. et al. Multicolor fluorescent switches in gel systems controlled by alkoxy chain and solvent. *Org. Biomol. Chem.* 2010; **8**(19): 4289-4296.
31. Martínez-Abadía M., Robles-Hernández B., de la Fuente M. R. et al. Photoresponsive Cyanostilbene Bent-Core Liquid Crystals as New Materials with Light-Driven Modulated Polarization. *Adv. Mater.* 2016; **28**(31): 6586-6591.
32. Peng X.-L., Ruiz-Barragan S., Ze-Sheng Li et al. Restricted access to a conical intersection to explain aggregation induced emission in dimethyl tetraphenylsilole. *J. Mater. Chem. C.* 2016; **4**(14): 2802-2810.
33. Martínez-Abadía M., Varghese S., Giménez R., and Ros M. B. Multiresponsive luminescent dicyanodistyrylbenzenes and their photochemistry in solution and in bulk. *J. Mater. Chem. C.* 2016; **4**(14): 2886-2893.
34. Oelkrug D., Tompert A., Gierschner J. et al. Tuning of Fluorescence in Films and Nanoparticles of Oligophenylenevinylenes. *J. Phys. Chem. B.* 1998; **102**(11): 1902-1907.
35. Souza M. M., Rumbles G., Gould I. R. et al. A theoretical and experimental study of cyano- and alkoxy-substituted phenylenevinylene model compounds. *Synth. Met.* 2000; **111/112**: 539-543.

36. Zhao C., Wang Z., Yang Y. et al. C–H••• π Interaction Induced Formation of Microtubes with Enhanced Emission. *Cryst. Growth Des.* 2012; **12**(3): 1227-1231.
37. Wang F., Han M.-Y., Mya K. Y. et al. Aggregation-Driven Growth of Size-Tunable Organic Nanoparticles Using Electronically Altered Conjugated Polymers. *J. Am. Chem. Soc.* 2005; **127**(29): 10350-10355.
38. Ito F., Sagawa T., and Koshiyama H. Fluorescence properties of nanoaggregates of pyrene ammonium derivative and its photoinduced dissolution and reaction in tetrahydrofuran/aqueous solutions. *Res. Chem. Intermed.* 2015; **41**(9): 6897-6906.
39. Barashkov N. N., Sakhno T. V., Nurmukhametov R. N., and Khakhel' O. A. Excimers of Organic Molecules. *Usp. Khim.* 1993; **66**(6): 579-593.
40. Ito F., Kakiuchi T., Sakano T., and Nagamura T. Fluorescence properties of pyrene derivative aggregates formed in polymer matrix depending on concentration. *Phys. Chem. Chem. Phys.* 2010; **12**(36): 10923-10927.
41. Sakhno T.V., Khakhel O.A., Barashkov N.N., Korotkova I.V. Excimer fluorescence of liquid crystalline systems. *Proceedings of SPIE - The International Society for Optical Engineering.* 1996; **2795**: 56-59.
42. Penn R. L. and Banfield J. F. Imperfect Oriented Attachment: Dislocation Generation in Defect-Free Nanocrystals. *Science.* 1998; **281**(5379): 969-971.
43. Qian Y., Li S., Zhang G. et al. Aggregation-Induced Emission Enhancement of 2-(2'-Hydroxyphenyl)benzothiazole-Based Excited-State Intramolecular Proton-Transfer Compounds. *J. Phys. Chem. B.* 2007; **111**(21): 5861-5868.
44. Sakhno T. V., Korotkova I. V., and Khakhel' O. A. Influence of temperature on quenching of fluorescence in compounds of the coumarin series. *Teor. Éksp. Khim.* 1996; **32**(4): 247-250.
45. Sakhno T. V., Korotkova I. V., and Khakhel' O. A. A possible mechanism of coumarin derivatives fluorescence quenching. *Funct. Mater.* 1996; **3**(4): 502-505.

46. Sakhno T. V., Korotkova I.V. and Barashkov N.N. The temperature dependence of radiation processes in 3,4-benzocoumarin. *Zh. Fiz. Khim.* 1997; **71**(5): 861-863.
47. Yan L. Q., Kong Z. N., Xia Y., and Qi Z. J. A novel coumarin-based red fluorogen with AIE, Self-assembly, and TADF properties. *New J. Chem.* 2016; **40**(8): 7061-7067.
48. Li S., He L., Xiong F. et al. Enhanced Fluorescent Emission of Organic Nanoparticles of an Intramolecular Proton Transfer Compound and Spontaneous Formation of One-Dimensional Nanostructures. *J. Phys. Chem. B.* 2004; **108**(30): 10887-10892.
49. Mei J., Leung N.L., Kwok R.T. et al. Aggregation-Induced Emission: Together We Shine, United We Soar! *Chem. Rev.* 2015; **115**(21): 11718-11940.
50. Liu B. and Zhang R. Aggregation induced emission: Concluding Remarks. *Faraday Discuss.* 2017; **196**: 461-472.
51. Hong Y., Lam J.W.Y., and Tang B.Z. Aggregation-induced emission: phenomenon, mechanism and applications. *Chem. Commun.* 2009; **29**: 4332-4353.
52. Bhongale C.J., Chang C.-W., Diao E. W.-G. et al. Formation of nanostructures of hexaphenylsilole with enhanced color-tunable emissions. *Chem. Phys. Lett.* 2006; **419**(4-6): 444-449.
53. Korotkova I.V., Sakhno T.V., Barashkov N.N. A quantum-chemical study of the influence of changes in the geometry of nitrogen-containing heterocyclic compounds on their fluorescent characteristics. *Russ J Phys Chem A.* 1999; **73**(1): 83-86.
54. Sakhno T.V., Korotkova I.V., Borisenko A.Yu., Pustovit S.V. Effect of temperature on the Fluorescence of O- and N-containing Heterocycles. XXth European Colloquium on Heterocyclic Chemistry, Stockholm, Sweden, August 18-21, 2002; 61.

55. Korotkova I.V., Sakhno T.V., Solov'ev V.V. Theoretical investigation of the solvent influence on the spectral-luminescent properties of molecules. *Ukrainian Chemistry Journal*. 1998; **64**(2): 9-13.
56. Nie H., Hu K., Cai Y. et al. Tetraphenylfuran: aggregation-induced emission or aggregation-caused quenching? *Mater. Chem. Front.* 2017; **1**(5): 1125-1129.
57. Zhang Y., Kong L., Shi J. et al. Aggregation-Induced Emission of Hexaphenyl-1,3-butadiene. *Chin. J. Chem.* 2015; **33**(7): 701-704.
58. Zhang Y., Mao H., Kong L. et al. Effect of E/Z Isomerization on the Aggregation-Induced Emission Features and Mechanochromic Performance of Dialdehyde-substituted Hexaphenyl-1,3-butadiene. *Dyes Pigments*. 2016; **133**: 354-362.
59. Mirochnik A.G., Fedorenko E.V., Gizzatulina D. Kh. and Karasev V. E. Photoinduced enhancement of luminescence from (dibenzoylmethanato)boron difluoride in polymethyl methacrylate. *Russ. J. Phys. Chem.* 2007; **81**: 1880-1883.
60. Tikhonov S.A., Vovna V.I., Osmushko I.S. et al. Boron difluoride dibenzoylmethane derivatives: Electronic structure and luminescence. *Spectrochim. Acta A*. 2018; **189**: 563-570.
61. Xu X., Chen S., Li L. et al. Photophysical properties of polyphenylphenyl compounds in aqueous solutions and application of their nanoparticles for nucleobase sensing. *J. Mater. Chem.* 2008; **18**(22): 2555-2561.
62. Rajagopal S.K., Philip A.M., Nagarajan K., and Hariharan M. Progressive acylation of pyrene engineers solid state packing and colour via C-H...H-C, C-H...O and π - π interactions. *Chem. Commun.* 2014; **50**(63): 8644-8647.
63. Rajagopan S.K., Reddy V.S., and Hariharan M. Crystallization Induced Green-Yellow-Orange Emitters Based on Benzoylpyrenes. *Cryst. Eng. Commun.* 2016; **18**(27): 5089-5094.
64. Feng C., Li J., Han X. et al. The E/Z Isomerization, Solvatochromism and Aggregation-induced Emission Enhancement of Donor-acceptor Type Oligo(pphenylene vinylene)s. *Faraday Discuss.* 2017; **196**: 163-176.

65. Samsonova L.G., Selivanov N.I. and Kopylova T.N. Spectral properties of Nile red in solutions and thin films. *Opt. Spectrosc.* 2014; **116**(1): 72–76. doi:10.1134/S0030400X14010196
66. Ferrer M.L. and del Monte F. Enhanced Emission of Nile Red Fluorescent Nanoparticles Embedded in Hybrid Sol-Gel Glasses. *J. Phys. Chem. B.* 2005; **109**(1): 80-86.
67. Quian G., Dai B., Luo M. et al. Band Gap Tunable, Donor-Acceptor-Donor Charge-Transfer Heteroquinoid-Based Chromophores: Near Infrared Photoluminescence and Electroluminescence. *Chem. Mater.* 2008; **20**(19): 6208-6216.
68. Tang W., Xiang Y., and Tong A. Salicylaldehyde Azines as Fluorophores of Aggregation-Induced Emission Enhancement Characteristics. *J. Org. Chem.* 2009; **74**(5): 2163-2166.
69. Cao X., Zeng Xi., Mu L. et al. Characterization of the aggregation-induced enhanced emission, sensing, and logic gate behavior of 2-(1-hydroxy-2-naphthyl)methylene hydrazine. *Sensors Actuators B.* 2013; **177**: 493-499.
70. Xiao H., Chen K., Cui D. et al. Two novel aggregation-induced emission active coumarin-based Schiff bases and their applications in cell imaging. *New J. Chem.* 2014; **38**(6): 2386-2393.
71. Niu C., Zhao L., Fang T. et al. Color- and Morphology-Controlled Self-Assembly of New Electron Donor-Substituted Aggregation-Induced Emission Compounds. *Langmuir.* 2014; **30**(9): 2351-2359.
72. Li J., Yang W., Zhou W. et al. Aggregation-induced emission in fluorophores containing hydrazone structure and sulfone central: restricted molecular rotation. *RSC Adv.* 2016; **6**(42): 35833-35841.
73. Luo J., Song K., Gu F. L. et al. Switching of non-helical overcrowded tetrabenzoheptafulvalene derivatives. *Chem. Sci.* 2011; **2**(10): 2029-2034.
74. Leung N.L. C., Xie N., Yuan W. et al. Restriction of Intramolecular Motions: The General Mechanism behind Aggregation-Induced Emission. *Chem. Eur. J.* 2014; **20**(47): 15349-15353.

75. Nishiuchi T., Tanaka K., and Kuwatani Y.Y. et al. Solvent-Induced Crystalline-State Emission and Multichromism of a Bent π -Surface System Composed of Dibenzocyclooctatetraene Units. *Chem. Eur. J.* 2013; **19**(13): 4110-4116.
76. Yuan C., Saito S., Camacho C. et al. Hybridization of a Flexible Cyclooctatetraene Core and Rigid Aceneimide Wings for Multiluminescent Flapping π Systems. *Chem. Eur. J.* 2014; **20**(8): 2193-2200.
77. Yuan C.-X., Tao X.-T., Ren Y. et al. Synthesis, Structure, and Aggregation-Induced Emission of a Novel Lambda (Λ)-Shaped Pyridinium Salt Based on Troger's Base. *J. Phys. Chem. C.* 2007; **111**(34): 12811-12816.
78. Liu J., Meng Q., Zhang X. et al. Aggregation-induced emission enhancement based on 11,11,12,12-tetracyano-9,10-anthraquinodimethane. *Chem. Commun.* 2013; **49**(12): 1199-1201.
79. Kamaldeep K.S.N., Kaur S., Bhalla V. et al. Pentacenequinone derivatives for preparation of gold nanoparticles: facile synthesis and catalytic application. *J. Mater. Chem. A.* 2014; **2**(22): 8369-8375.
80. Kaur S., Gupta A., Bhalla V. et al. Pentacenequinone derivatives: aggregation-induced emission enhancement, mechanism and fluorescent aggregates for superamplified detection of nitroaromatic explosives. *J. Mater. Chem. C.* 2014; **2**(35): 7356-7363.
81. Aguilar-Granda A., Pérez-Estrada S., Roa A. E. et al. Synthesis of a Carbazole-[π]-carbazole Molecular Rotor with Fast Solid State Intramolecular Dynamics and Crystallization-Induced Emission. *Cryst. Growth Des.* 2016; **16**(6): 3435-3442.
82. Cariati E., Lanzeni V., Tordin E. et al. Efficient crystallization induced emissive materials based on a simple push-pull molecular structure. *Phys. Chem. Chem. Phys.* 2011; **13**(40): 18005-18014.
83. Wang B., Wang X., Wang W. and Liu F. Exploring the Mechanism of Fluorescence Quenching and Aggregation-Induced Emission of a Phenylethylene Derivative by QM (CASSCF and TDDFT) and

- ONIOM(QM:MM) Calculations. *J. Phys. Chem. C.* 2016; **120**(38): 21850-21857.
84. Hestand N.J. and Spano F.C. Molecular Aggregate Photophysics beyond the Kasha Model: Novel Design Principles for Organic Materials. *Accounts Chem. Res.* 2017; **50**(2): 341-350.
85. Gruzecki W.I. Structural Characterization of the Aggregated Forms of Violaxanthin. *J. Biol. Phys.* 1991; **18**(2): 99-109.
86. Gruzecki W. I., Zelent B., and Leblanc R. M. Fluorescence of zeaxanthin and violaxanthin in aggregated forms. *Chem. Phys. Lett.* 1990; **171**(5/6): 563-568.
87. Ramesh N. and Patnaik A. Iso-oriented Fluorescent Colloidal Nanocrystals of Bis-cyanostyryl Thiophenes: Crucial Secondary Halogen Interactions towards Stability and Transport. *J. Phys. Chem. C.* 2016; **120**(3): 1909-1917.
88. Muentner A. A., Brumbaugh D. V., Apolito J. J. et al. Size Dependence of Excited-State Dynamics for J-Aggregates at AgBr Interfaces. *J. Phys. Chem.* 1992; **96**(7): 2783-2790.
89. Gierschner J. and Park S.Y. Luminescent distyrylbenzenes: tailoring molecular structure and crystalline morphology. *J. Mater. Chem. C.* 2013; **1**(37): 5818-5832.
90. Nikolenko L.M. and Ivanchikhina A.V. Features of J-aggregate of cyanine dyes formation in solutions of AOT /Water/Hexane reverse micels. *Khim. Vysok. Énerg.* 2010; **44**(6): 1-9.
91. Bhattacharyya B., Kundu A., Das A. et al. One-pot protocol for J-aggregated anthraimidazolediones catalyzed by phosphotungstic acid in PEG-400 under aerobic condition. *RSC Adv.* 2016; **6**(26): 21907-21916.
92. Nosova D.A., Zarochentseva E.P., Vysotskaya S.O. et al. Influence of Crystalline Structure on Aggregate-Induced Luminescence of Aminobenzoic Acid Derivatives. *Opt. Spektroskop.* 2014; **117**(6): 907-913.
93. Shapiro B.I., Sokolova L.S., Kuz'min V.A. et al. Effect of meso-alkyl substituents in the polymethine chain of thiocarbocyanines on the morphology

- of dye aggregates. *Nanotechnol Russia*. 2012; **7**(5/6): 205–212. doi:10.1134/S1995078012030159
94. An B.-K., Gierschner J., and Park S. Y. π -Conjugated Cyanostilbene Derivatives: A Unique Self-Assembly Motif for Molecular Nanostructures with Enhanced Emission and Transport. *Accounts Chem. Res.* 2012; **45**(4): 544-554.
95. Ozcelik S. and Akins D. L. Superradiance of Aggregated Thiocarbocyanine Molecules. *J. Phys. Chem. B*. 1999; **103**(42): 8926-8929.
96. Zhang B., Diao W., Bi C. et al. Donor-Acceptor Compound Based on Rhodanineacetic Acid-Pyrene Derivative: Red-Light Emitting Fluorescent Organic Nanoparticles. *J. Fluoresc.* 2012; **22**(1): 1-7.
97. Sakhno T.V., Korotkova I.V., Barashkov N.N., and Ferraris J. P. Optical properties of some polyphenylvinylene. *Proceedings of SPIE - The International Society for Optical Engineering*. 1997; **3488**: 284-292.
98. Lange F., Hohnholz D., Leuze M. et al. Structural influences on luminescence properties of substituted ppvs and model compounds. *Synth. Met.* 1999; **101**(1): 652-653.
99. Lamère J.F., Saffon N., Santos I.D., and Fery-Forgues S. Aggregation-Induced Emission Enhancement in Organic Ion Pairs. *Langmuir*. 2010; **26**(12): 10210-10217.
100. Ravotto L. and Ceroni P. Aggregation induced phosphorescence of metal complexes: From principles to applications *Coordination Chemistry Reviews*. *Coord. Chem. Rev.* 2017; **346**: 62-76.
101. Sathish V., Ramdass A., Thanasekaran P., and Lu K.-L. Aggregation-induced phosphorescence enhancement (AIPE) based on transition metal complexes – An overview. *J. Photochem. Photobiol. C*. 2015; **23**: 25-44.
102. Jiang Y., Li G., Che W. et al. A neutral dinuclear Ir(III) complex for anti-counterfeiting and data encryption. *Chem. Commun.* 2017; **53**(21): 3022-3025.

103. Shan G.G., Li H.B., Qin J.S. et al. Piezochromic luminescent (PCL) behavior and aggregation-induced emission (AIE) property of a new cationic iridium(III) complex. *Dalton Trans.* 2012; **41**(32): 9590-9593.
104. Li G. F., Wu Y., Shan G. G. et al, New ionic dinuclear Ir(III) Schiff base complexes with aggregation-induced phosphorescent emission (AIPE). *Chem. Commun.* 2014; **50**(53): 6977-6980.
105. Thanasekaran P., Wu J. Y., Manimaran B. et al. Aggregate of Alkoxy-Bridged Re(I)-Rectangles as a Probe for Photoluminescence Quenching. *J. Phys. Chem. A.* 2007; **111**(43): 10953-10960.
106. Granchak V. M., Sakhno T. V., and Kuchmy S. Ya. Light-Emitting Materials – Active Components of Luminescent Solar Concentrators. *Teor. Éksp. Khim.* 2014; **50**(1): 1-20.
107. Banal J.L., White J.M., Ghiggino K. P. et al. Concentrating Aggregation-Induced Fluorescence in Planar Waveguides: A Proof-of-Principle. *Sci. Rep.* 2014; **4**: 4635.
108. Kok-Haw Ong and Bin Liu. Applications of Fluorogens with Rotor Structures in Solar Cells. *Molecules.* 2017; **22**(6): 897.
109. Feng G., Ryan T.K.K., Tang B.Z., and Liu B. Functionality and versatility of aggregation-induced emission luminogens. *Appl. Phys. Rev.* 2017; **4**: 021307.
110. Banal J.L., Ghiggino K.P. and Wong W.W.H. Efficient light harvesting of a luminescent solar concentrator using excitation energy transfer from an aggregation-induced emitter. *Phys. Chem. Chem. Phys.* 2014; **16**(46): 25358-25363.
111. Banal J.L., White J.M., Lam T.W. et al. A Transparent Planar Concentrator Using Aggregates of gem-Pyrene Ethenes. *Adv. Energy Mater.* 2015; **5**: 1500818.
112. Banal J.L., Soleimaninejad H., Jradi F.M. et al. Energy Migration in Organic Solar Concentrators with a Molecularly Insulated Perylene Diimide. *J. Phys. Chem. C.* 2016; **120**(24): 12952-12958.

113. Zhang B., Banal J. L., Jones D. J. et al, Aggregation-induced emission-mediated spectral downconversion in luminescent solar concentrators. *Mater. Chem. Front.* 2018; **2**(3): 615-619.
114. Zhao Z. J., Lam J.W.Y., and Tang B.Z. Tetraphenylethene: a versatile AIE building block for the construction of efficient luminescent materials for organic light-emitting diodes. *J. Mater. Chem.* 2012; **22**(45): 23726-23740.
115. Liu Y.H, Mu C., Jiang K. et al. A tetraphenylethylene core-based 3D structure small molecular acceptor enabling efficient non-fullerene organic solar cells. *Adv. Mater.* 2015; **27**(6): 1015-1020.
116. Hong Y. Aggregation-induced emission-fluorophores and applications. *Methods Appl. Fluoresc.* 2016; **4**: 022003.
117. Qin W., Yang Z., Jiang Y. et al. Construction of Efficient Deep Blue Aggregation-Induced Emission Luminogen from Triphenylethene for Nondoped Organic Light-Emitting Diodes. *Chem. Mater.* 2015; **27**(11): 3892-3901.
118. Liu B., Nie H., Zhou X. et al. Manipulation of Charge and Exciton Distribution Based on Blue Aggregation-Induced Emission Fluorophors: A Novel Concept to Achieve High-Performance Hybrid White Organic Light-Emitting Diodes. *Adv. Function. Mater.* 2016; **26**(5): 776-783.
119. Xie Z. L., Chen C. J., Xu S. D. et al. White-light emission strategy of a single organic compound with aggregation-induced emission and delayed fluorescence properties. *Angew. Chem. Int. Ed.* 2015; **54**(24): 7181-7184.
120. Zhao D., Fan Fan, Cheng Juan et al. Light-Emitting Liquid Crystal Displays Based on an Aggregation-Induced Emission Luminogen. *Adv. Opt. Mater.* 2015; **3**(2): 199-202.
121. Liu J., Su H., Meng L. et al. What makes efficient circularly polarised luminescence in the condensed phase: aggregation-induced circular dichroism and light emission. *Chem. Sci.* 2012; **3**(9): 2737-2747.

122. Zhang G., Zhang X., Zhang Y. et al. Design of turn-on fluorescent probe for effective detection of Hg^{2+} by combination of AIEE-active fluorophore and binding site. *Sensors Actuators B*. 2015; **221**: 730-739.
123. Huerta-Aguilar C. A., Raj P., Thangarasu P. and Singh N. Fluorescent organic nanoparticles (FONs) for selective recognition of Al^{3+} : application to bio-imaging for bacterial sample. *RSC Adv*. 2016; **6**(44): 37944-37952.
124. Tang Guo, Xiaozheng Cao, Peng Ge et al. A self-assembled fluorescent organic nanoprobe and its application for sulfite detection in food samples and living systems. *Org. Biomol. Chem*. 2017; **15**(20): 4375-4382.
125. Malakar A., Kumar M., Reddy A. et al. Aggregation induced enhanced emission of 2-(2'-hydroxyphenyl)benzimidazole. *Photochem. Photobiol. Sci*. 2016; **15**(7): 937-948.
126. Dan Wang, Shu-Mu Li, Jian-Quan Zheng et al. Coordination-Directed Stacking and Aggregation-Induced Emission Enhancement of the Zn(II) Schiff Base Complex. *Inorg. Chem*. 2017; **56**(2): 984-990.
127. Li Y.R., Zhou H.T., Chen W. et al. A simple AIE-based chemosensor for highly sensitive and selective detection of Hg^{2+} and CN^- . *Tetrahedron*. 2016; **72**(36): 5620-5625.
128. Tian T., Chen X., Li H. et al. Amidine-based fluorescent chemosensor with high applicability for detection of CO_2 : A facile way to "see" CO_2 . *Analyst*. 2013; **138**(4): 991-994.
129. Han T., Lam J.W., Zhao N. et al. A fluorescence-switchable luminogen in the solid state: a sensitive and selective sensor for the fast "turn-on" detection of primary amine gas. *Chem. Commun*. 2013; **49**(42): 4848-4850.
130. Cai Y., Li L., Wang Z. et al. A sensitivity tuneable tetraphenylethene-based fluorescent probe for directly indicating the concentration of hydrogen sulfide. *Chem. Commun*. 2014; **50**(64): 8892-8895.
131. Wang J. H., Feng H. T., and Zheng Y. S. *Chem. Commun*. 2014; **50**(77): 11407-11410.

132. Zhang R., Cai X., Feng G., and Liu B. Real-time naked-eye multiplex detection of toxins and bacteria using AIEgens with the assistance of graphene oxide. *Faraday Discuss.* 2017; **196**: 363-375.
133. Korneev O.V., Sakhno T.V., Korotkova I.V. Nanoparticles-based photosensitizers with effect of aggregation-induced emission. *Biopolymers and Cell.* 2019; **35**(4): 249–267.
134. Raab O. Über die Wirkung fluorescieren der Stoffe auf Infusorien. *Ztg Biol.* 1900; **39**: 524–526.
135. Von Tappeiner H, Jesionek H. Therapeutische versuche mit fluoreszierenden stoffen. *Munch Med Wochenschr.* 1903; **47**: 2042–2044.
136. Von Tappeiner H.A., Jodlbauer A. Die Sensibilisierende Wirkung Fluorescierender Substanzen: Gesammelte Untersuchungen Über die Photodynamische Erscheinung. Leipzig, Germany: F.C.W. Vogel, 1907: 210 p.
137. Dougherty T.J., Grindey G.B., Fiel R., Weishaupt K.R., Boyle D.G. Photoradiation therapy. II. Cure of animal tumors with hematoporphyrin and light. *J Natl Cancer Inst.* 1975; **55**(1):115–121.
138. Dougherty T.J. Photodynamic therapy - new approaches. *Semin Surg Oncol.* 1989; **5**(1): 6–16.
139. Kennedy J.C., Marcus S.L., Pottier R.H. Photodynamic therapy (PDT) and photodiagnosis (PD) using endogenous photosensitization induced by 5-aminolevulinic acid (ALA): mechanisms and clinical results. *J Clin Laser Med Surg.* 1996; **14**(5): 289–304.
140. Stennett E.M., Ciuba M.A., Levitus M. Photophysical processes in single molecule organic fluorescent probes. *Chem Soc Rev.* 2014; **43**(4):1057–1075.
141. Korotkova I.V., Sakhno T.V., Barashkov N.N. Theoretical study of radiationless deactivation of a series of coumarin derivatives. *Theor Exp Chem.* 1997; **33**(2): 90–94.
142. Barashkov N.N., Korotkova I.V., Sakhno T.V. Spectral manifestations of aggregates structure of heteroaromatic molecules at low temperatures. *J Lumin.* 2000; **87-89**: 794–796.

143. Novikova T. S., Sakhno T. V., Korotkova I.V. et al. Spectral properties of polymer composition based on Polyvinylalcohol. *Polymer Journal* (18181724). 2011; **33**(1): 261-267.
144. Plotnikov V.G. Theoretical foundations of the classification of molecules by luminescence spectra. *Russ Chem Rev.* 1980; **49**(2): 172–189.
145. Rabahi A., Makhloufi-Chebli M., Zaater S. Synthesis, characterisation, estimation of ground-and excited-state dipole moments using solvatochromic shift and theoretical studies of new iminocoumarin derivatives. *Journal of Molecular Structure.* 2019; **1181**: 270-278.
146. Das A.K., Goswami S., Dolai M. Design, synthesis and structural optimization of two click modified butterfly molecules: Aggregation induced ratiometric fluorescence change and ICT associated hydrogen bonding effect in solvatochromic analysis. *Journal of Molecular Structure.* 2019; **1181**: 329-337
147. Grynyov B.V., Sakhno T.V., Senchishin V.G. Optically transparent and fluorescent polymers. *Kharkiv Institute of single crystals* 2003; 575 p.
148. Muehlmann L.A., Ma B.C., Longo J.P., Almeida Santos Mde F., Azevedo R.B. Aluminum-phthalocyanine chloride associated to poly(methyl vinyl ether-co-maleic anhydride) nanoparticles as a new third-generation photosensitizer for anticancer photodynamic therapy. *Int J Nanomedicine.* 2014; **9**: 1199–1213.
149. Foote C.S. Definition of type I and type II photosensitized oxidation. *Photochem Photobiol.* 1991; **54**(5): 659.
150. Hamblin M.R., Newman E.L. On the mechanism of the tumour-localising effect in photodynamic therapy. *J Photochem Photobiol B.* 1994; **23**(1): 3–8.
151. Hudson R., Boyle R.W. Strategies for selective delivery of photodynamic sensitisers to biological targets. *J Porphyr Phthalocyanines.* 2004; **8**(7): 954–975.

152. Minaev B.F., Yashchuk L.B. Possible electronic mechanisms of generation and quenching of luminescence of singlet oxygen in the course of photodynamic therapy: ab initio study. *Biopolym Cell*. 2006; **22**(3): 231–235.
153. Bregnhøj M., Westberg M., Minaev B.F., Ogilby P.R. Singlet oxygen photophysics in liquid solvents: converging on a unified picture. *Acc Chem Res*. 2017; **50**(8):1920–1927.
154. Minaev B.F. Electronic mechanisms of molecular oxygen activation. *Russ Chem Rev*. 2007; **76**(11): 988–1010.
155. Minaev B. Photochemistry and spectroscopy of singlet oxygen in solvents. Recent advances which support the old theory. *Chem Chem Tech*. 2016; **10**(4S): 519-530.
156. Abrahamse H., Hamblin M.R. New photosensitizers for photodynamic therapy. *Biochem J*. 2016; **473**(4): 347–364.
157. Triesscheijn M., Baas P., Schellens J.H., Stewart F.A. Photodynamic therapy in oncology. *Oncologist*. 2006; **11**(9): 1034–1044.
158. Allison R.R., Downie G.H., Cuenca R., Hu X.H., Childs C.J., Sibata C.H. Photosensitizers in clinical PDT. *Photodiagnosis Photodyn Ther*. 2004; **1**(1): 27–42.
159. Allison R.R., Moghissi K. Photodynamic therapy (PDT): PDT mechanisms. *Clin Endosc*. 2013; **46**(1): 24–29.
160. van Straten D., Mashayekhi V., de Bruijn H.S., Oliveira S., Robinson D.J. Oncologic Photodynamic therapy: basic principles, current clinical status and future directions. *Cancers (Basel)*. 2017; **9**(2). pii: E19.
161. Yi G., Hong S.H., Son J., Yoo J., Park C., Choi Y., Koo H. Recent advances in nanoparticle carriers for photodynamic therapy. *Quant Imaging Med Surg*. 2018; **8**(4): 433–443.
162. Lipson R.L., Baldes E.J. The photodynamic properties of a particular hematoporphyrin derivative. *Arch Dermatol*. 1960; **82**: 508–516.

163. Dougherty T.J., Kaufman J.E., Goldfarb A., Weishaupt K.R., Boyle D., Mittleman A. Photoradiation therapy for the treatment of malignant tumors. *Cancer Res.* 1978; **38**(8): 2628–2635.
164. Taratula O., Schumann C., Duong T., Taylor K.L., Taratula O. Dendrimer-encapsulated naphthaloc naphthalocyanine as a single agent-based theranostic nanoplatform for near-infrared fluorescence imaging and combinatorial anticancer phototherapy. *Nanoscale.* 2015; **7**(9): 3888–3902.
165. Allémann E., Rousseau J., Brasseur N., Kudrevich S.V., Lewis K., van Lier J.E. Photodynamic therapy of tumours with hexadecafluoro zinc phthalocynine formulated in PEG-coated poly(lactic acid) nanoparticles. *Int J Cancer.* 1996; **66**(6): 821–824.
166. Moghimi S.M., Hunter A.C., Murray J.C. Long-circulating and target-specific nanoparticles: theory to practice. *Pharmacol Rev.* 2001; **53**(2): 283–318.
167. Kim H., Chung K., Lee S., Kim D.H., Lee H. Near-infrared light-responsive nanomaterials for cancer theranostics. *Wiley Interdiscip Rev Nanomed Nanobiotechnol.* 2016; **8**(1): 23–45.
168. Gamaleia N.F., Shton I.O. Gold mining for PDT: Great expectations from tiny nanoparticles. *Photodiagnosis Photodyn Ther.* 2015; **12**(2): 221–31.
169. Hong S.H., Kim H., Choi Y. Indocyanine green-loaded hollow mesoporous silica nanoparticles as an activatable theranostic agent. *Nanotechnology.* 2017; **28**(18): 185102.
170. Chen B., Pogue B.W., Hasan T. Liposomal delivery of photosensitising agents. *Expert Opin Drug Deliv.* 2005; **2**(3): 477–487.
171. Hadinoto K., Sundaresan A., Cheow W.S. Lipid-polymer hybrid nanoparticles as a new generation therapeutic delivery platform: a review. *Eur J Pharm Biopharm.* 2013; **85**(3 Pt A): 427–443.
172. Hong E.J., Choi D.G., Shim M.S. Targeted and effective photodynamic therapy for cancer using functionalized nanomaterials. *Acta Pharm Sin B.* 2016; **6**(4): 297–307.

173. Son J., Yang S.M., Yi G., Roh Y.J. et al. Folate-modified PLGA nanoparticles for tumor-targeted delivery of pheophorbide a in vivo. *Biochem Biophys Res Commun.* 2018; **498**(3): 523–528.
174. Yoon H.Y., Koo H., Choi K.Y. et al. Tumortargeting hyaluronic acid nanoparticles for photodynamic imaging and therapy. *Biomaterials.* 2012; **33**(15): 3980–3989.
175. Granchak V.M., Sakhno T.V., Korotkova I.V., Sakhno Yu.E., Kuchmy S.Ya. Aggregation-induced emission in organic nanoparticles: properties and applications: a review. *Theoretical and Experimental Chemistry.* 2018; **54**(3): 147–77.
176. Behera S.. K., Murkherjee A., Sadhuragiri G. et al. Aggregation induced enhanced and exclusively highly Stokes shifted emission from an excited state intramolecular proton transfer exhibiting molecule. *Faraday Disc.* 2017; **196**: 71-90.
177. Manikandan I., Chang C.H. and Chen C.L. Aggregation induced emission enhancement (AIEE) characteristics of quinoline based compound - A versatile fluorescent probe for pH, Fe(III) ion, BSA binding and optical cell imaging. *Spectrochim. Acta A.* 2017; **182**: 58-66.
178. Qin W., Dan D., Liu J. Z. et al. Biocompatible Nanoparticles with Aggregation-Induced Emission Characteristics as Far-Red/Near-Infrared Fluorescent Bioprobes for In Vitro and In Vivo Imaging Applications. *Adv. Funct. Mater.* 2012; **22**(4): 771-779.
179. Li K., Qin W., Ding D. et al., Photostable fluorescent organic dots with aggregation-induced emission (AIE dots) for noninvasive long-term cell tracing. *Sci. Rep.* 2013; **3**: 1150-1156.
180. Feng G., Liu B. Aggregation-Induced Emission (AIE) Dots: Emerging Theranostic Nanolights. *Acc. Chem. Res.* 2018; **51**(6): 1404-1414
181. Ding D., Mao D., Li K. et al. Precise and Long-Term Tracking of Adipose-Derived Stem Cells and Their Regenerative Capacity *via* Superb Bright and Stable Organic Nanodots. *ACS Nano.* 2014; **8**(12): 12620-12631.

182. Yan L. L., Zhang Y., Xu B. et al. Fluorescent nanoparticles based on AIE fluorogens for bioimaging. *Nanoscale*. 2016; **8**(5): 2471-2487.
183. Liu J., Chen C., Ji S. et al. Long wavelength excitable near-infrared fluorescent nanoparticles with aggregation-induced emission characteristics for image-guided tumor resection. *Chem. Sci*. 2017; **8**(4): 2782-2789.
184. Qin W., Dan D., Liu J., Yuan W. et al. Biocompatible nanoparticles with aggregation-induced emission characteristics as far-red/near-infrared fluorescent bioprobes for in vitro and in vivo imaging applications. *Adv Funct Mater*. 2012; **22**(4): 771–779.
185. Yuan Y., Feng G., Qin W., Tang B.Z., Liu B. Targeted and image-guided photodynamic cancer therapy based on organic nanoparticles with aggregation-induced emission characteristics. *Chem Commun (Camb)*. 2014; **50**(63): 8757–60.
186. Li M., Gao Y., Yuan Y., Wu Y. Et al. One-step formulation of targeted aggregation-induced emission dots for image-guided photodynamic therapy of cholangiocarcinoma. *ACS Nano*. 2017; **11**(4): 3922–3932.
187. Feng G., Qin W., Hu Q., Tang B.Z., Liu B. Cellular and mitochondrial dual-targeted organic dots with aggregation-induced emission characteristics for image-guided photodynamic therapy. *Adv Healthc Mater*. 2015; **4**(17): 2667–76.
188. Shi H., Liu J., Geng J. et al. Specific detection of integrin $\alpha v \beta 3$ by light-up bioprobe with aggregation-induced emission characteristics. *J. Am. Chem. Soc*. 2012; **134**(23): 9569-9572.
189. Shi H., Kwok R.T., Liu J. et al. Real-Time Monitoring of Cell Apoptosis and Drug Screening Using Fluorescent Light-Up Probe with Aggregation-Induced Emission Characteristics. *J. Am. Chem. Soc*. 2012; **134**(43): 17972-17981.
190. Ding D., Li K., Liu B., and Tang B. Z. Bioprobes based on AIE fluorogens. *Accounts Chem. Res*. 2013; **46**(11): 2441-2453.

191. Kwok R.T., Leung C.W., Lam J.W. et al. Biosensing by luminogens with aggregation-induced emission characteristics. *Chem. Soc. Rev.* 2015; **44**(13): 4228-4238.
192. Yuan Y.Y., Zhang C., Gao M. et al. Specific Light-Up Bioprobe with Aggregation-Induced Emission and Activatable Photoactivity for the Targeted and Image-Guided Photodynamic Ablation of Cancer Cells. *Angew. Chem. Int. Ed.* 2015; **54**(6): 1780-1786.
193. Yuan Y.Y., Xu S.D., Cheng X.M. et al. Bioorthogonal Turn-On Probe Based on Aggregation-Induced Emission Characteristics for Cancer Cell Imaging and Ablation. *Angew. Chem. Int. Ed.* 2016; **55**(22): 6457-6461.
194. Hu F., Huang Y.Y., Zhang G. X. et al. Targeted Bioimaging and Photodynamic Therapy of Cancer Cells with an Activatable Red Fluorescent Bioprobe. *Anal. Chem.* 2014; **86**(15): 7987-7995.
195. Yuan Y.Y., Zhang C. J., Xu S. D., and Liu B. A self-reporting AIE probe with a built-in singlet oxygen sensor for targeted photodynamic ablation of cancer cells. *Chem. Sci.* 2016; **7**(3): 1862-1866.
196. Feng G.X., Yuan Y.Y., Fang H. et al. A light-up probe with aggregation-induced emission characteristics (AIE) for selective imaging, naked-eye detection and photodynamic killing of Gram-positive bacteria. *Chem. Commun.* 2015; **51**(62): 12490-12493.
197. Zhao E.G., Chen Y. L., Chen S. J. et al. A Luminogen with Aggregation-Induced Emission Characteristics for Wash-Free Bacterial Imaging, High-Throughput Antibiotics Screening and Bacterial Susceptibility Evaluation. *Adv. Mater.* 2015; **27**(33): 4931-4937.
198. He X., Xiong L.-H., Zhao Z., Wang Z. et al. AIE-based theranostic systems for detection and killing of pathogens. *Theranostics.* 2019; **9**(11): 3223-3248.
199. Hu F., Manghnani P.N., Kenry, Feng G. et al. Visualize Embryogenesis and Cell Fate Using Fluorescent Probes with Aggregation-Induced Emission. *ACS Appl. Mater. Interfaces.* 2019; **11**: 3737-3744

200. Jayaram D.T., Ramos-Romero S., Shankar B.H. et al. In vitro and in vivo demonstration of photodynamic activity and cytoplasm imaging through the nanoparticles. *ACS Chem Biol.* 2016; **11**(1): 104–112.
201. Perry S.W., Norman J.P., Barbieri J., Brown E.B., Gelbard H.A. Mitochondrial membrane potential probes and the proton gradient: a practical usage guide. *Biotechniques.* 2011; **50**(2): 98–115.
202. Zhao N., Chen S., Hong Y., Tang B.Z. A red emitting mitochondria-targeted AIE probe as an indicator for membrane potential and mouse sperm activity. *Chem Commun (Camb).* 2015; **51**(71):13599–602.
203. Gu B., Wu W., Xu G., Feng G. et al. Precise Two-photon photodynamic therapy using an efficient photosensitizer with aggregation-induced emission characteristics. *Adv Mater.* 2017; **29**(28). doi: 10.1002/adma.201701076
204. Guan Y., Lu H., Li W., Zheng Y., Jiang Z., Zou J., Gao H. Near-infrared triggered upconversion polymeric nanoparticles based on aggregation-induced emission and mitochondria targeting for photodynamic cancer therapy. *ACS Appl Mater Interfaces.* 2017; **9**(32): 26731–26739.
205. Zheng Y., Lu H., Jiang Z., Guan Y., Zou J., Wang X., Cheng R., Gao H. Low-power white light triggered AIE polymer nanoparticles with high ROS quantum yield for mitochondria-targeted and image-guided photodynamic therapy. *J Mater Chem B.* 2017; **5**(31): 6277–81.
206. Decock J., Obermajer N., Vozelj S., Hendrickx W., Paridaens R., Kos J. Cathepsin B, cathepsin H, cathepsin X and cystatin C in sera of patients with early-stage and inflammatory breast cancer. *Int J Biol Markers.* 2008; **23**(3): 161–168.
207. Yuan Y., Zhang C.J., Gao M., Zhang R., Tang B.Z., Liu B. Specific light-up bioprobe with aggregation-induced emission and activatable photoactivity for the targeted and image-guided photodynamic ablation of cancer cells. *Angew Chem Int Ed Engl.* 2015; **54**(6): 1780–1786.

208. Han K., Wang S.B., Lei Q., Zhu J.Y., Zhang X.Z. Ratiometric Biosensor for Aggregation-induced emission-guided precise photodynamic therapy. *ACS Nano*. 2015; **9**(10):10268–10277.
209. Sun X., Zebibula A., Dong X., Li G., Zhang G. et al. Targeted and imaging-guided in vivo photodynamic therapy of tumors using dualfunctional, aggregation-induced emission nanoparticles. *Nano Research*. 2018; **11**(5): 2756–2770.
210. Chen K., Zhang R., Wang Z. et al. Structural Modification Orientated Multifunctional AIE Fluorescence Probes: Organelles Imaging and Effective Photosensitizer for Photodynamic Therapy. *Adv. Optical Mater.* 2019; 1901433 doi: 10.1002/adom.201901433
211. Alam P., Dash S., Climent C., Kaur G., Choudhury A.R. et al. Aggregation-induced emission' active iridium(III) complexes with applications in mitochondrial staining. *RSC Adv*. 2017; **7**: 5642–5648.
212. Ndagi U., Mhlongo N., and Soliman M.E. Metal complexes in cancer therapy – an update from drug design perspective. *Drug Des Devel Ther.* 2017; **11**: 599–616.
213. Liu Y., Song N., Chen L., Xie Z-G. BODIPY@Ir(III) complexes assembling organic nanoparticles for enhanced photodynamic therapy. *Chin J Polymer Sci*. 2018; **36**(3): 417–424.
214. Zou J., Xue L., Yang N., Ren Y. et al. Glutathione Responsive Pyrrolopyrrolidone Nanotheranostic Agent for Turn-on Fluorescence Imaging Guided Photothermal/ Photodynamic Cancer Therapy. *Mater. Chem. Front*. 2019; doi: 10.1039/C9QM00471H.]

FOR AUTHOR USE ONLY

**More
Books!**



yes
I want morebooks!

Buy your books fast and straightforward online - at one of world's fastest growing online book stores! Environmentally sound due to Print-on-Demand technologies.

Buy your books online at
www.morebooks.shop

Kaufen Sie Ihre Bücher schnell und unkompliziert online – auf einer der am schnellsten wachsenden Buchhandelsplattformen weltweit! Dank Print-On-Demand umwelt- und ressourcenschonend produziert.

Bücher schneller online kaufen
www.morebooks.shop

KS OmniScriptum Publishing
Brivibas gatve 197
LV-1039 Riga, Latvia
Telefax: +371 686 20455

info@omniscryptum.com
www.omniscryptum.com

OMNIscriptum



FOR AUTHOR USE ONLY